A resonant response of the California Current circulation to forcing by low frequency climate variability

William J. Crawford[a,*], Andrew M. Moore[a], Michael G. Jacox[b,c], Jérôme Fiechter[a], Emilie Neveu[d], Christopher A. Edwards[a]

[a] Department of Ocean Sciences, University of California, 1156 High Street, Santa Cruz, CA 95062, United States
[b] Institute of Marine Sciences, University of California, 1156 High Street, Santa Cruz, CA 5062, United States
[c] Environmental Research Division, Southwest Fisheries Science Center, NOAA, Monterey, California
[d] INRIA, Rhonˆe-Alpes Research Center, Grenoble, France

ARTICLE INFO

ABSTRACT

Low frequency variability of the California Current System (CCS) is investigated using circulation estimates based on a 31-year (1980–2010) sequence of historical analyses of the CCS calculated using the Regional Ocean Modeling System (ROMS) 4-dimensional variational (4D-Var) data assimilation system. The leading 3-dimensional multivariate empirical orthogonal functions (3D EOFs) of the CCS circulation were computed and provide a detailed view of low-frequency circulation variability within the CCS. The 3D EOFs are used as basis functions for a linear inverse model of the circulation, and several Principal Oscillation Patterns (POPs) of the circulation are identified. The leading POPs have periods in the range $\sim 4 - 10$ years, and shed light on the 3-dimensional time evolving structure associated with low-frequency variability in the circulation. A particular focus here is coastal upwelling. In particular, a POP with a period close to 10 years appears to be preferentially excited as a resonant response to forcing associated with the regional expression of the Pacific Decadal Oscillation, the North Pacific Gyre Oscillation and the El Niño Southern Oscillation.

1. Introduction

The California Current is one of four major eastern boundary currents in the global ocean characterized by a pronounced seasonal cycle of coastal upwelling. Primary productivity in the California Current System (CCS) supports an important and diverse complex of marine ecosystems that are vulnerable to climate variability and climate change. The CCS circulation is characterized by variability on space- and time-scales ranging from the relatively short, sub-seasonal variability of the sub-mesoscale circulation, through to seasonal, inter-annual, and decadal time-scales. The CCS is arguably one of the best observed regions of the world ocean. Nevertheless, despite the plethora of ocean observations along the U.S. west coast, the *in situ* observations are fairly sparse in space and time, and large swaths of the ocean surface are often obscured by an extensive layer of marine stratus, preventing infrared sensors aboard earth orbiting satellites from observing the surface temperature. Data assimilation is therefore an important tool for blending discontinuous ocean observations with state-of-the-art ocean models to yield reliable space-time estimates of the circulation. Neveu et al. (2017) hereafter N16 describe in detail a sequence of ocean

circulation estimates for the CCS that span the last three decades, and that are based on an advanced 4-dimensional variational (4D-Var) data assimilation system. The circulation estimates described in N16 are available as a community resource, and in this paper they are used to quantify the variability in the CCS circulation associated with the Pacific Decadal Oscillation (PDO), the North Pacific Gyre Oscillation (NPGO), and, to a lesser degree, ENSO.

The NPGO is the oceanic complement of the atmospheric North Pacific Oscillation and is characterized by a spin-up and spin-down of the subtropical and subpolar gyre circulations on decadal time-scales (Di Lorenzo et al., 2008). The NPGO index is defined as the Principal Component (PC) time series of the second EOF of SSH in the North Pacific (http://www.o3d.org/npgo). Since the CCS forms part of the equatorward branch of the North Pacific subtropical gyre, the NPGO can significantly influence the coastal circulation along the U.S. west coast. The positive phase of the NPGO manifests itself physically as a strengthening of the North Pacific Current characterized by an increase in the meridional sea surface height (SSH) gradient, downwelling favorable conditions in the subtropical gyre and along the Alaskan coast, and upwelling favorable conditions in the Alaskan gyre and in the CCS

---

* Corresponding author.
  E-mail address: wjcrawfo@ucsc.edu (W.J. Crawford).

equatorward of 38 °N (Di Lorenzo et al., 2008).

Within the CCS region, the NPGO has been shown to correlate with variability in sea surface salinity (SSS), nutrients, chlorophyll-a, and alongshore upwelling winds (Di Lorenzo et al., 2009; Chhak et al., 2009a, 2009b). Combes et al. (2013) confirmed the connection between the NPGO and upwelling winds by correlating the surface concentration of a modeled passive tracer along the central and southern California coast (following a sub-surface release) with the NPGO index. Additionally, Chenillat et al. (2012) have shown that the phase of the NPGO can affect the timing of the onset of the upwelling season (i.e. the spring transition), with the positive (negative) phase initiating an earlier (delayed) onset. The timing of the spring transition has been shown to have significant ecological effects with an early onset of upwelling typically leading to a more productive ecosystem (McClatchie et al., 2009).

The PDO is another important basin-wide mode of variability, with a structure similar to the El Niño Southern Oscillation (ENSO) in the tropical central and eastern Pacific (Mantua et al., 1997). Similar to ENSO, the PDO drives variability through adjustments to the atmospheric pressure over the North Pacific and is defined as the first PC time series of SST in the North Pacific between 20° N and 65˚N (http://jisao.washington.edu/pdo). During the positive phase of the PDO, anomalously low pressure in the North Pacific is associated with cyclonic winds along the west coast of North America. Poleward alongshore wind anomalies drive anomalous onshore transport of surface water creating anomalously high sea surface temperature (SST) and SSH. Schneider and Cornuelle (2005) have shown that the PDO can be viewed as the combined response of ocean forcing by ENSO and the Aleutian Low, and modulation of zonal advection by the Kuroshio-Oyashio extension by oceanic Rossby waves, lending weight to the idea that the PDO is not associated with a single dynamical mode of the ocean-atmosphere system.

The influence of the low-frequency component of the PDO on the CCS is commonly discussed in terms of regime shifts. A shift in phase (or polarity) of the PDO often leads to a shift in the long-term average (>10 years) of the ocean state that is generally accompanied by a shift in ecological communities. Such a regime shift occurred in 1977 when the PDO transitioned from a negative to positive phase accompanied by anomalously low sea level pressure leading to weakened alongshore winds, warm SST anomalies and anomalously high SSH in the CCS (Miller et al., 1994; King, 2005). Bograd and Lynn (2003) document a warming in the upper 200–400 m of the water column, an increase in stratification, and shifts in the position of the dominant large-scale currents in the CCS due to changes in the depth and slope of isopycnal surfaces. The PDO has also been linked with the source depth of coastally upwelled waters, with the positive phase leading to a reduction in source depth (Chhak and Di Lorenzo, 2007). This reduction in the supply of deep, nutrient rich waters during the positive phase of the PDO is coherent with changes in marine ecosystem communities during the 1977 regime shift (McGowan et al., 2003; Chavez et al., 2003).

More recently, Johnstone and Mantua (2014) have explored the role of the PDO in the context of the observed long term upward trend in SST in the Northeast Pacific between 1900 and 2012 (Field et al., 2006) and its connection to anthropogenic forcing. They found that even though an upward trend is apparent in sea level pressure and SST, a *possible* reversal of the trend has occurred since 1980.

The CCS response to ENSO is driven by two distinct mechanisms often referred to as *local* and *oceanic* mechanisms. The local forcing of ENSO on the CCS is through atmospheric teleconnections from the tropics which drive changes in the local atmospheric circulation. The oceanic forcing occurs via coastally trapped waves that propagate poleward along the coastal wave guide from the equator. A frequently used index of ENSO activity in the equatorial Pacific is the Multivariate ENSO Index (MEI, http://www.esrl.noaa.gov/psd/enso/mei). The MEI is defined as the principal component (PC) time series of the first EOF of a combination of several measured oceanic and atmospheric variables

in the tropical Pacific that include sea-level pressure, SST, zonal and meridional components of the surface wind, surface air temperature and total cloudiness (Wolter and Timlin, 2011).

The PDO and NPGO are essentially statistical constructs and have been identified from EOF analyses of surface fields alone. However, this view of the oceanic and atmospheric circulation is far from complete and may very well represent a very distorted view of the circulation variability in regions such as the CCS. In this paper, we have adopted a different approach to that commonly used, and explore variability in CCS circulation estimates by considering covariability in the full 3-dimensional ocean circulation. The ocean circulation estimates used here span the period 1980–2010 and were computed using the Regional Ocean Modeling System (ROMS) and a 4D-Var data assimilation system. The ROMS-CCS 4D-Var analysis system is briefly reviewed in Section 2. In Section 3, multivariate 3-dimensional principal component analysis is used to explore the dominant spatial modes of variability captured by the 4D-Var analyses. In Section 4, the Principal Oscillation Patterns (POPs) of the CCS circulation are computed using linear inverse modeling methods, and in Section 5 are used to explore the intrinsic low frequency variability of coastal upwelling. Specifically forcing of the leading POPs by the PDO, NPGO and ENSO is explored. A summary of our findings and conclusions is presented in Section 6.

2. The CCS historical analyses

The CCS circulation estimates analyzed here were computed by assimilating available observations for the period 1980–2010 into ROMS using 4D-Var data assimilation. The configuration of the model and ROMS 4D-Var data assimilation system are presented in detail in N16, so only a brief description will be given here.

The ROMS CCS model domain and bathymetry are illustrated in Fig. 1. The model was configured with 1/10° horizontal resolution and 42 terrian following σ-levels in the vertical that vary in thickness between 0.3 m and 8 m over the continental shelf and 7–100 m in the deep ocean. The period 1980–2010 was divided into consecutive 8-day overlapping windows, and all available ocean observations during each window were assimilated into ROMS CCS. Observations assimilated
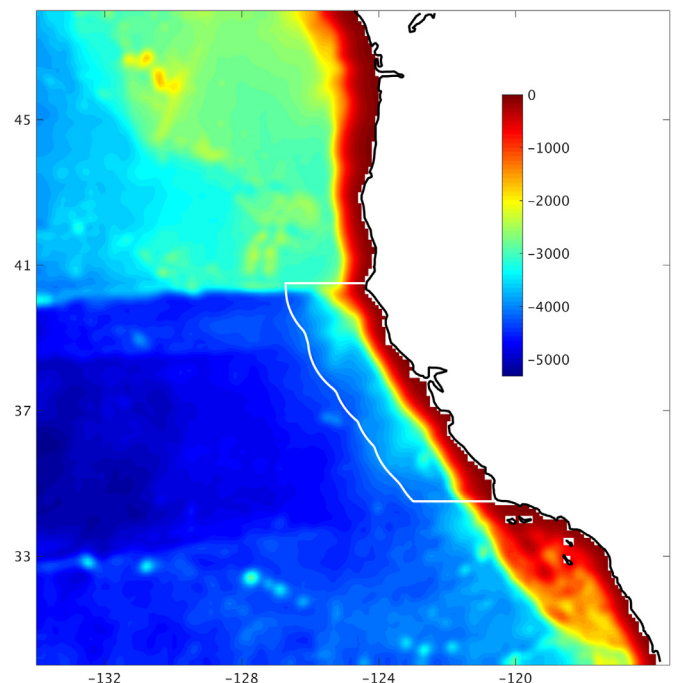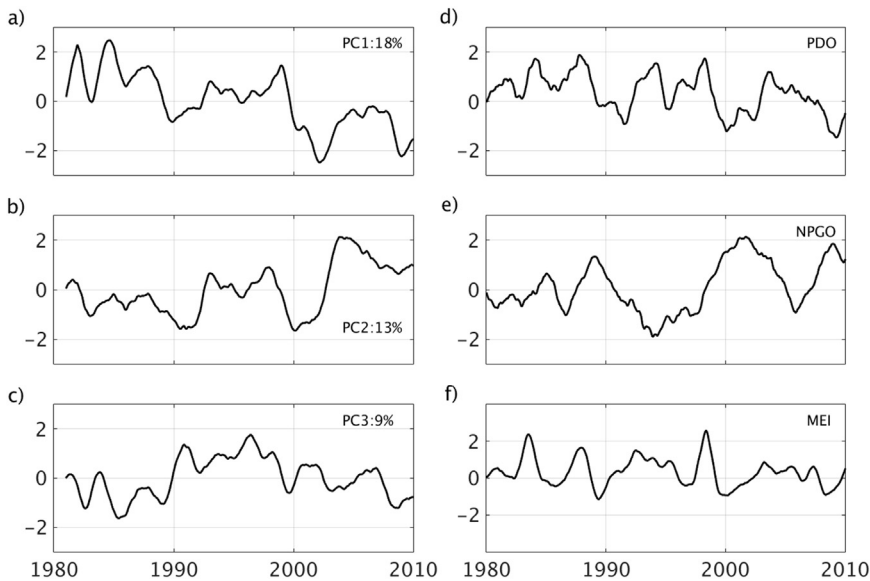

Fig. 1. The ROMS domain and bathymetry (m) used in WCRA31. Also shown is the central California region referred to in the text, which extends offshore 200 km between Cape Mendocino and Point Conception.

Fig. 2. Principal component time series for the leading three 3D EOFs of WCRA31 (a) r_1, (b) r_2, and (c) r_3. Time series of (d) the PDO index, (e) the NPGO index, and (f) the MEI. A 12-month running mean has been applied to each time series.

include satellite SST (AVHRR, MODIS and AMSR-E), SSH (Aviso), and in situ hydrographic profiles of temperature and salinity. During each data assimilation cycle, the initial conditions, surface and open boundary conditions were adjusted using the 4D-Var procedure. The prior (or background) state for the initial conditions was taken to be the posterior (or analysis) at the mid-point of the previous cycle. The prior surface forcing was derived from a combination of sources which include atmospheric variables at standard height from the ECMWF 40-year reanalysis (ERA40) (1980–2001; Källberg et al., 2004) and ERA Interim products (2002–2010; Dee et al., 2011), and surface winds from the Cross-Calibrated Multi-Platform (CCMP) ocean wind product of Atlas et al. (2011). The prior open boundary conditions were taken from the global Simple Ocean Data Assimilation product (SODA) of Carton and Giese (2008). The resulting 4D-Var circulation analyses spanning the 31-year period will be referred to in sequel as WCRA31.

3. Multivariate 3D EOF analysis

3.1. Computation of the EOFs

Since the majority of ocean observations take the form of satellite measurements of SST and SSH, it is common to compute Empirical Orthogonal Functions (EOFs) of surface data alone. The leading EOFs of observed SST and SSH within the ROMS domain of Fig. 1 yield spatial patterns of variance that share features in common with published EOFs of SST and SSH for the entire North Pacific (not shown). Specifically, the regional EOFs capture some of the features in SST and SSH associated with the PDO, the NPGO and ENSO along the U.S. west coast. The associated PC time series of the leading two EOFs of observed SST and SSH correlate quite well with the generally accepted indicators of the PDO, NPGO and ENSO (not shown). However, EOF calculations of observed SST and SSH that are limited to the model domain are unable to completely describe the regional expressions of the basin-wide EOFs that define the PDO and NPGO.

The 4D-Var analyses, however, provide a complete space-time view of the ocean circulation. Therefore, we are not restricted to exploring only surface variability and, as we will demonstrate, restricting attention to the surface circulation alone may lead to a distorted view of the circulation variability, since the surface conditions describe only a small subset of the entire circulation conditions and account for a small fraction of the ocean energy. A unique aspect of the current work is the computation of multivariate 3-dimensional (3D) EOFs of the circulation using all grid point values of the ROMS temperature, salinity, velocity

and sea surface displacement, which provide a much more complete view of the CCS circulation variability than 2D EOFs of surface fields.

The 3D multivariate EOFs were computed for WCRA31 using monthly averaged fields as described in Appendix A. Prior to computing the EOFs, each 4D-Var analysis field was spatially smoothed using 20 applications of a 2nd-order Shapiro filter in order to suppress the influence of the mesoscale circulations on the covariance. In conjunction with the monthly averaging this procedure approximates low-pass filtering of the time series of 4D-Var analyses in the frequency-wave-number domain, with the purpose of highlighting the low-frequency, large-scale components of circulation variability that is the focus here. The resulting 3D multivariate covariance matrix has a dimension $\sim 5.5 \times 10^6$ so standard matrix algorithms cannot be used to compute the EOFs. Instead, the leading EOFs were computed using an iterative Lanczos method (Golub and Van Loan, 1989), which is also described in Appendix A.

3.2. Climate indicators and correlations

While the EOFs of the covariance matrix, **C** (cf Appendix A), represent the leading modes of variability in the model domain only, it is of interest to quantify the extent to which these patterns of regional circulation correlate with ENSO, the PDO and the NPGO. Time series of the PDO index, the NPGO index and the MEI for the period spanned by WCRA31 are shown in Fig. 2d–f for reference, where each time series has been smoothed using a 12-month running mean.

We will focus primarily on the leading three EOFs, which are denoted r_1, r_2 and r_3 following the notation of Appendix A. Correlations of the PC time series of r_1, r_2 and r_3 with each climate index are shown in Table 1 along with the percentage of the energy density that is explained. PC1 is significantly correlated with all three climate indices,

Table 1
The percentage of variance explained by each of the leading three multivariate 3D EOFs of WCRA31. Also shown are the correlation coefficients between the PC time series associated with each EOF and the PDO index, the NPGO index and the MEI. All significant correlations are shown in bold face.

PC	1	2	3
%	18%	13%	9%
PDO	**0.70**	**0.25**	0.10
NPGO	**− 0.54**	− 0.13	**− 0.45**
MEI	**0.35**	0.16	0.29

and particularly with the PDO and NPGO. The correlation of PC2 with each index is quite low, while PC3 captures some of the variance associated with the NPGO. The fraction of variance explained by the leading 3D EOFs ranges between 18% and 9%, consistent with a 3D EOF spectrum that is relatively flat (see Appendix A, Fig. A.2). This may be partly due to the very large dimension of the model state. However, subsampling the 4D-Var circulation fields at lower resolution (20 km, 30 km and 50 km were considered here) yields the same EOFs and the same explained variance, despite the dramatic reduction in dimension (not shown). Therefore the relatively flat EOF spectrum must be associated with the wide range of 3D circulation structures that are present in the 4D-Var analyses.

Table 1 indicates that the 3D circulation variability in the CCS is considerably more complicated than the conventional view based on the PDO and NPGO modes of variability identified based solely on surface fields of SST and SSH (both of which account for a small fraction of the total energy density - see Appendix A, Eq. (A.2)). The structure of the leading three 3D EOFs will be considered next.

3.3. CCS EOFs

3.3.1. EOF 1 ($\mathbf{r}_1$)

The PC time series of the leading EOF $\mathbf{r}_1$ is shown in Fig. 2a and $\mathbf{r}_1$ explains 18% of the energy density. The most significant characteristic of the first PC time series in Fig. 2a is the downward trend over the length of the analysis time period. The SST and SSH structure of $\mathbf{r}_1$ are shown in Fig. 3a. In combination, Fig. 2a and Fig. 3a indicate that prior to 2000, the SST and SSH associated with $\mathbf{r}_1$ were mostly positive throughout the domain, however the downward trend in the PC time series corresponds to a surface cooling along the coast (~ 0.3 °C), and a lowering of sea level (~ 1 cm) during the most recent decade of WCRA31 relative to the mean associated with $\mathbf{r}_1$.

Fig. 3d shows the sea surface salinity (SSS) and surface circulation of $\mathbf{r}_1$, and in combination with Figs. 2a and Fig. 3a indicates cooler (warmer) by ~ 0.5 °C than normal surface conditions along the coast during the period 2000–2010 (1980–1999) associated with $\mathbf{r}_1$, accompanied by surface salinities that were higher (lower) by ~ 0.1 psu than

the mean. At the same time, $\mathbf{r}_1$ acts to weaken the equatorward California Current poleward of Cape Mendocino (Fig. 3d) during the most recent decade and strengthens it prior to 2000.

The vertical structure of temperature and salinity associated with $\mathbf{r}_1$ over the upper 500 m of the water column is shown in Figs. 4a and d, and reveals that the largest temperature and salinity anomalies are found offshore at depths near the pycnocline. The downward trend in temperature during the analysis period ($\sim 1 - 1.5$ °C in total above the thermocline) associated with $\mathbf{r}_1$ (Fig. 2a) is coherent across the entire domain, whereas salinity associated with $\mathbf{r}_1$ increased within ~ 500 km of the coast by ~ 0.2 psu and decreased within the subtropical gyre by a similar amount. The upward trending salinity anomalies near the coast associated with $\mathbf{r}_1$ may be related to adjustments in the source depth during ENSO events (Jacox et al., 2015) which act to force the PDO (Newman et al., 2003; Schneider and Cornuelle, 2005).

3.3.2. EOF 2 ($\mathbf{r}_2$)

The PC time series for $\mathbf{r}_2$ is shown in Fig. 2b. There is a relatively high correlation with the PC time series of $\mathbf{r}_1$ (0.74) at a lag of about 3 years which is quite evident by comparing Figs. 2b and a. As demonstrated in Section 4, $\mathbf{r}_1$ and $\mathbf{r}_2$ are companion EOFs that describe the variance associated with several oscillatory dynamical modes.

The SST, SSH and SSS associated with $\mathbf{r}_2$ are shown in Figs. 3b and e, respectively. EOF $\mathbf{r}_2$ accounts for 13% of the energy density, and its corresponding PC time series exhibits low frequency variability with sign changes every 5–10 years, similar to $\mathbf{r}_1$ (Fig. 2b). During much of the 1990s and the 2000s, the PC time series of $\mathbf{r}_2$ was positive (Fig. 2b), corresponding to surface conditions associated with $\mathbf{r}_2$ that were warmer and fresher than the mean over much of the domain with near normal SST and SSS along the coast, and a stronger (weaker) California Current equatorward (poleward) of Cape Mendocino (Fig. 3e). Conversely during the 1980s and early 2000s, the anomalous conditions associated with $\mathbf{r}_2$ were reversed. Typical offshore SST and SSS anomalies associated with $\mathbf{r}_2$ are ~ 0.3 °C and 0.07 psu. The vertical structure of $\mathbf{r}_2$ is shown in Figs. 4b and e and reveals that surface temperature anomalies extend well below the surface and change sign around 100–200 m depth. Salinity variations are also broadly coherent
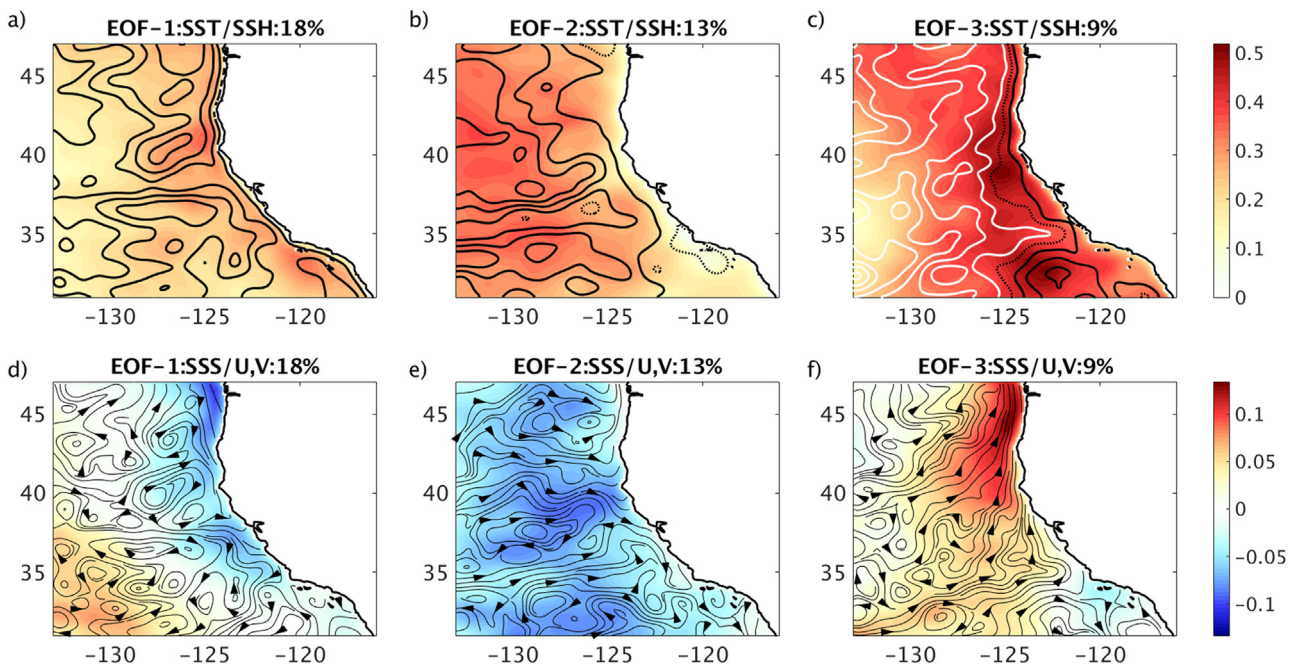

Fig. 3. The SST (color), SSH (contours), SSS (color) and surface circulation (streamlines) associated with the leading three EOFS of WCRA31: (a,d) $\mathbf{r}_1$, (b,e) $\mathbf{r}_2$, and (c,f) $\mathbf{r}_3$. The percentage of explained variance of the energy density Tr($\mathbf{C}_1$) is also indicated. The color bars are in units of degrees Celsius or psu, while the contour interval is 5×10^{-3} m. Black (white) contours indicate positive (negative) values of SSH. (For interpretation of the references to color in this figure legend, the reader is referred to the web version of this article.)
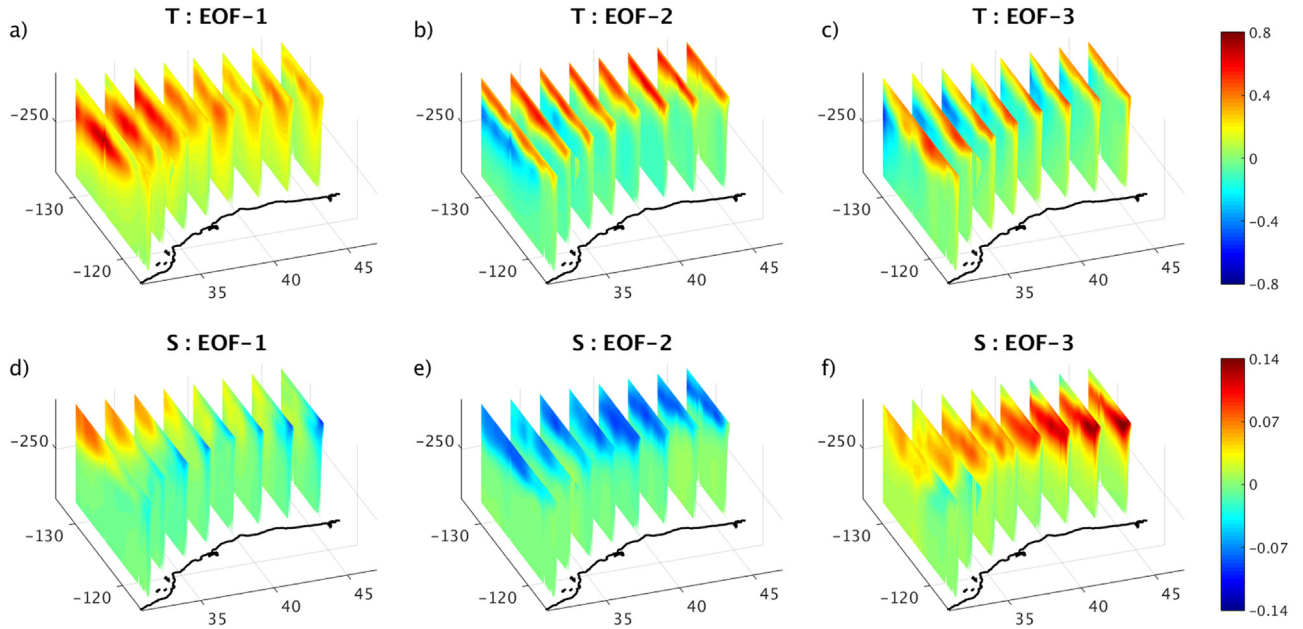
Fig. 4. Vertical zonal sections over the upper 500 m of the water column along every 2 degrees of latitude of temperature (*T*) and salinity (*S*) for the leading three EOFs of WCRA31: (a,d) $\mathbf{r}_1$, (b,e) $\mathbf{r}_2$, and (c,f) $\mathbf{r}_3$.

over the whole domain down to 200–300 m where there is a change in sign. Typical $\mathbf{r}_2$ subsurface temperature and salinity anomalies are $\sim 0.5\,°C$ and ~ 0.1 psu.

3.3.3. EOF 3 ($\mathbf{r}_3$)

EOF $\mathbf{r}_3$ accounts for 9% of the energy density, and the SST, SSH and SSS for $\mathbf{r}_3$ are shown in Figs. 3c and f. Like $\mathbf{r}_1$, SST is single signed across the entire domain, and decreases in amplitude offshore, while SSS for $\mathbf{r}_3$ changes sign in the Southern California Bight (SCB). During the 1990s, the PC time series associated with $\mathbf{r}_3$ was positive (Fig. 2c) and accompanied by warmer than normal conditions ($\sim 0.4\,°C$) along the entire coast, more saline conditions poleward of Cape Mendocino (~ 0.1 psu), near average SSS along the central California coast, and slightly fresher conditions in the SCB (~ 0.02 psu) associated with $\mathbf{r}_3$. The component of the California Current associated with $\mathbf{r}_3$ (Fig. 3f) was weaker than average along the entire coast. The temperature and salinity anomalies associated with $\mathbf{r}_3$ exhibit quite complex vertical structures as shown in Figs. 4c and f. Temperature changes sign at around 200 m depth, except along the coast. However, over the upper 100 m or so, temperature and salinity anomalies associated with $\mathbf{r}_3$ have the same sign, suggesting that they influence the spiciness of the ocean (i.e. density variations due to changes in temperature and salinity act to cancel each other out) rather than density.

4. Linear inverse modeling of the ccs

While the 3D-EOFs shed light on the dominant patterns of variance in the 3D-circulation, they do not, in general, provide direct information about the spatial structure of inherent dynamical modes of the system (e.g. Dommenget and Latif, 2002; Monahan and Fyfe, 2006; Monahan et al., 2009). A powerful method for uncovering the dynamical modes is linear inverse modeling which is an attempt to construct a low-dimensional approximation of the full dynamical operators that govern the evolution of the circulation in space and time. An excellent review of linear inverse modeling can be found in von Storch et al. (1995), and there are many notable applications in the atmospheric, oceanic and climate sciences (e.g. Penland, 1989; Penland and Magorian, 1993; Penland and Ghil, 1993; Penland and Sardeshmukh, 1995; Del Sole and Hou, 1999; Moore and Kleeman, 2001; Winkler et al., 2001).

Following the notation in Appendix A, let $\overline{\mathbf{x}}$ represent the time mean ocean state, and $\delta\mathbf{x} = \mathbf{x} - \overline{\mathbf{x}}$ denote departures of $\mathbf{x}$ from the mean. If $\delta\mathbf{x}$ is in statistical equilibrium, the hypothesis set forth in linear inverse modeling is that $\delta\mathbf{x}$ can be modeled as a stable, stochastically forced, linear system (i.e. as a first-order autoregressive or Markov process), so that:

$$d\delta\mathbf{x} = \mathbf{A}\delta\mathbf{x}dt + \xi dt \tag{1}$$

where $\mathbf{A}$ is the dynamical system matrix that describes the time rate of change of $\delta\mathbf{x}$, and ξdt is a white noise (in time) stochastic forcing. The eigenvectors of $\mathbf{A}$ are the normal modes of the system, and are of considerable interest because they represent the dynamical modes of the circulation variability about the mean (Pedlosky, 1979). For large dimensional systems like that considered here, direct computation of the normal modes from (1) is very challenging. However, the normal modes can be approximated using a linear inverse model (LIM) representation of the 4D-Var analyses time series. The procedure used here is described in detail in Appendix B, and uses the leading 3D multivariate EOFs and associated PC time series of Section 3 to compute a reduced rank approximation $\widetilde{\mathbf{M}}$ of $\mathbf{A}$. Specifically, if $\mathbf{u}(t)$ denotes the vector of PC time series of the leading 3D EOFs, then:

$$\widetilde{\mathbf{M}} = \mathbf{\Phi}(t + \tau)\mathbf{\Phi}(t)^{-1} \tag{2}$$

where $\mathbf{\Phi}(t) = \langle \mathbf{u}(t)\mathbf{u}^T(t)\rangle$ and $\mathbf{\Phi}(t + \tau) = \langle \mathbf{u}(t + \tau)\mathbf{u}^T(t)\rangle$ represent the zero-lag and time-lagged covariance matrices of $\mathbf{u}(t)$ respectively, and τ is the time lag. The eigenvectors of $\widetilde{\mathbf{M}}$ represent empirical approximations of the normal modes, and are referred to as Principal Oscillation Patterns (POPs; Hasslemann, 1988). The underlying hypotheses behind (1) can be tested (Penland and Sardeshmukh, 1995) as described in Appendix C.

4.1. Principal oscillation patterns of the CCS

As described in Appendix C, the PC time series associated with the leading 3D EOFs identified in Section 3 (cf Fig. 2) were used to compute the leading POPs of the CCS circulation. The underlying hypotheses of the linear inverse modeling approach were rigorously tested as described in Appendix C, and were by-and-large found to be satisfied for the LIMs considered here. Here we will focus on the results obtained from a particular choice of parameters, but note that the results are

relatively insensitive to the parameters chosen (see Appendix C, Section C.1). The POPs described here were computed after the linear trend was removed from each PC time series. This was done to minimize any aliasing or ambiguity that may arise in the period of the POPs associated with the trends in the time series. In addition, each PC time series was smoothed using a 12-month running mean. While this last step is not essential (see Appendix C), it generally leads to a better separation of eigenmodes within the POP spectrum, and eliminates non-oscillating modes which are probably non-physical. For the POPs presented here, we used a time-lag of $\tau = 6$ months in (2), and the leading 10 3D EOFs which account for 57% of the energy density (cf Appendix A).

The POPs are identified from the eigenvector equation $\widetilde{\mathbf{M}}\mathbf{e}_i = \lambda_i \mathbf{e}_i$, where in general the eigenvalues λ_i and eigenvectors $\mathbf{e}_i$ are complex. Each POP, $\hat{\mathbf{u}}$, evolves in time according to $\hat{\mathbf{u}}_i(t) = e^{\lambda_i t}\mathbf{e}_i$, where λ_i is the complex frequency such that $Re(\lambda_i)$ is the POP decay rate and $Im(\lambda_i)$ is the oscillatory frequency. Since $\widetilde{\mathbf{M}}$ in (2) is derived from stationary time series, then by necessity $Re(\lambda_i) < 0$ for all POPs (Penland and Sardeshmukh, 1995). Both λ_i and $\mathbf{e}_i$ typically occur in complex conjugate pairs, and for $N = 10$, there will be five complex conjugate pairs of POPs. Table 2 shows the period and e-folding decay time of the five pairs of POPs in this case. The POPs have periods that range from 3.6 years to 40.6 years. Even though the original time series only span a period of 31 years, it is still possible for the POPs to have a period that exceeds the length of the time series (e.g. non-oscillating POPs have an infinite period). The e-folding times range from 1.1 to 9.6 years. The POP of particular interest here is mode 3 with a period of 9.7 years and a long e-folding decay time of 9.6 years, since this POP can dominate the stochastically forced response of the system (1), as demonstrated in Section 4.2. Table 2 shows that POP 4 also has a period close to 10 years, but this mode decays very quickly, and is typically much less important (and unreliable as demonstrated below).

The amplitude of each POP is given by $a_i(t) = (\mathbf{e}_i^\dagger)^H \delta\mathbf{x}^T(t)$ where $\mathbf{e}_i^\dagger$ are the eigenvectors of $\widetilde{\mathbf{M}}^T$, and superscript H denotes the Hermitian transpose. The amplitude coefficients $a_i(t)$ will, in general, be complex and the real and imaginary components should mimic the properties of true dynamical normal modes of the system. In particular, as discussed by von Storch et al. (1995), the coherence and phase of $Re(a_i(t))$ and $Im(a_i(t))$ can be used to decide whether a particular POP describes a true physical mode. Figs. 5a–c show the cross-power spectra between $Re(a_i(t))$ and $Im(a_i(t))$ for the leading three POPs, and reveals that in each case it peaks at or very near the period of the mode based on λ, as expected for a normal mode. Also shown in Figs. 5a–c is the squared coherence between $Re(a_i(t))$ and $Im(a_i(t))$ which is also high over a range of frequencies close to the POP period, a property also exhibited by normal modes. In addition, Figs. 5d–f show the phase difference between $Re(a_i(t))$ and $Im(a_i(t))$ which is close to $-90°$ in the vicinity of the POP frequency, as required.[1] Therefore, according to Fig. 5 the amplitudes of POPs 1, 2 and 3 generally have properties that mimic those of real dynamical modes. However, the coherence and/or phase of POPs 4 and 5 do not, in general, display these same properties (not shown) so should be treated with caution (von Storch et al., 1995).

Our focus here will be on low frequency variability of the circulation in the central California region, which is controlled primarily by POP 3. Fig. 6 shows the real and imaginary components of SST, SSH, SSS and the surface circulation associated with POP 3. As POP 3 evolves in time, the circulation is described by the sequence $Re(\mathbf{e}_3) \rightarrow -Im(\mathbf{e}_3) \rightarrow -Re(\mathbf{e}_3) \rightarrow Im(\mathbf{e}_3) \rightarrow Re(\mathbf{e}_3) \rightarrow ....$ Apart from an arbitrary difference in sign, the real components of the SST and SSS of POP 3 are similar to that of EOF $\mathbf{r}_2$ (Fig. 3) since POP 3 projects most on this EOF (see Table 2). The imaginary components, however, are distinct and represent a superposition of several EOFs. Fig. 6 indicates that as POP 3 evolves in time, a uniformly cool sea surface (Fig. 6a) gives

---

[1] The real and imaginary components of a normal mode represent the quadrature phases of the mode.

Table 2
Period and e-folding decay time (years) for the five POPs (ordered according to increasing period) for the case $\tau = 6$, $N = 10$. Also shown is the projection of each POP on the leading three 3D EOFs.

POP	Period (yrs)	Decay time (yrs)	r_1	r_2	r_3
1	3.6	2.2	0.65	0.13	0.49
2	5.2	2.7	0.59	0.55	0.23
3	9.7	9.6	0.53	0.62	0.33
4	9.9	1.1	0.63	0.37	0.45
5	40.6	3.9	0.23	0.28	0.76

way to near normal conditions over much of the domain one quarter of a period later (∼ 2.4 years) with warming near 132°W, 45°N (the negative of Fig. 6b). Warmer conditions spread primarily from the north west and south east across the entire region during the next quarter period (the negative of Fig. 6a) to be replaced by near normal SST except near 45°N where the surface cools (Fig. 6b), after which the cycle repeats itself. During the same cycle, higher than normal SSS (Fig. 6c) over much of the domain becomes concentrated between Cape Blanco and Cape Mendocino (the negative of Fig. 6d) then give way to less saline conditions across the domain (the negative of Fig. 6c) before becoming concentrated between Cape Blanco and Cape Mendocino (Fig. 6d).

In Section 5 we will focus specifically on upwelling variability along the central California coast. Therefore, we will focus here in detail on the circulation variability in this same region. Fig. 7 shows the 3-dimensional temperature, salinity and velocity structure of the oscillatory component of $\mathbf{e}_3$ (i.e. the decaying component has been suppressed) during one complete period over the upper 200 m of the water column in the region $36°N - 44°N$, $122° - 126°W$ spanning the central California coast. Fig. 7 reveals that the progression of surface temperature and salinity anomalies described in relation to Fig. 6 is coherent over the upper water column, and undergo a sign change near the thermocline. The subsurface anomalies evident in Fig. 7 are coherent across the entire model domain (not shown). The relative phase between the different components of the circulation is illustrated in Fig. 8 in the form of Hovmoller diagrams along 38°N, spanning the entire model domain, and for two cycles of $\mathbf{e}_3$, again with the decaying component of the POP suppressed. The 38°N line is near the southern end of the region shown in Fig. 7, although the Hovmoller diagrams in Fig. 8 are representative of the phase relations within the whole region. Variations in temperature (Fig. 8b) and salinity (Fig. 8c) are generally in phase across the entire model domain, with cooler (warmer) conditions associated with more (less) saline surface waters consistent with Figs. 6 and 7. SST also exhibits a slight eastward phase propagation (Fig. 8b). In Fig. 8a variations in the depth of the $\sigma = 26\,\mathrm{kgm}^{-3}$ isopycnal surface are used as a proxy for changes in the depth of the main thermocline, and west of 127°W are out of phase with SST and SSS by about 1/4 cycle. East of 127°W Fig. 8a shows that anomalies in thermocline depth display an westward phase propagation, and are more in phase with variations in SST and SSS near the coast. The progression of temperature and salinity anomalies east of 127°W associated with $\mathbf{e}_3$ through one cycle in Fig. 7 are therefore accompanied by a low frequency "sloshing" of the thermocline. While Figs. 7b and c show that cold temperature anomalies progressively give way to warm anomalies in the upper 100 m east of 127°W, Fig. 8a shows that the thermocline generally remains shallower than normal away from the coast (consistent with cold temperature anomalies below 100 m). These warm anomalies (and the associated salinity anomalies) appear to propagate in to the region from the north west and south east as described in relation to Figs. 6a and b. During this time Figs. 7b and c indicate that the California Current appears to weaken, first at the surface, and then at depth also. Fig. 8d suggests that movements of the thermocline near the coast are preceded by approximately one quarter of a period by changes in vertical velocity adjacent to the coast. The largest variations
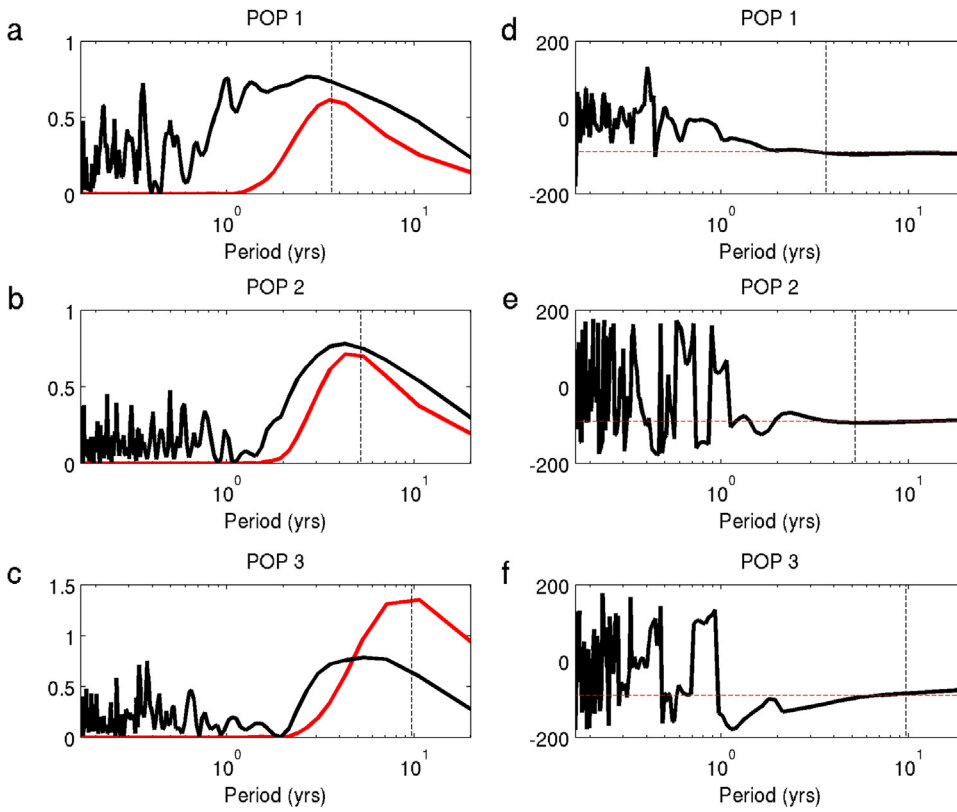
Fig. 5. The cross-power spectral density between the real and imaginary components of the mode amplitudes (red curves) and the squared coherence (black curves) for POPs 1, 2 and 3 are shown in (a), (b) and (c) versus period. The phase difference (degrees) between the real and imaginary components of the POP amplitudes are shown in (d), (e) and (f). The black dashed line indicates the period of the POPe and the red dashed line denotes a − 90° phase difference. (For interpretation of the references to color in this figure legend, the reader is referred to the web version of this article.)
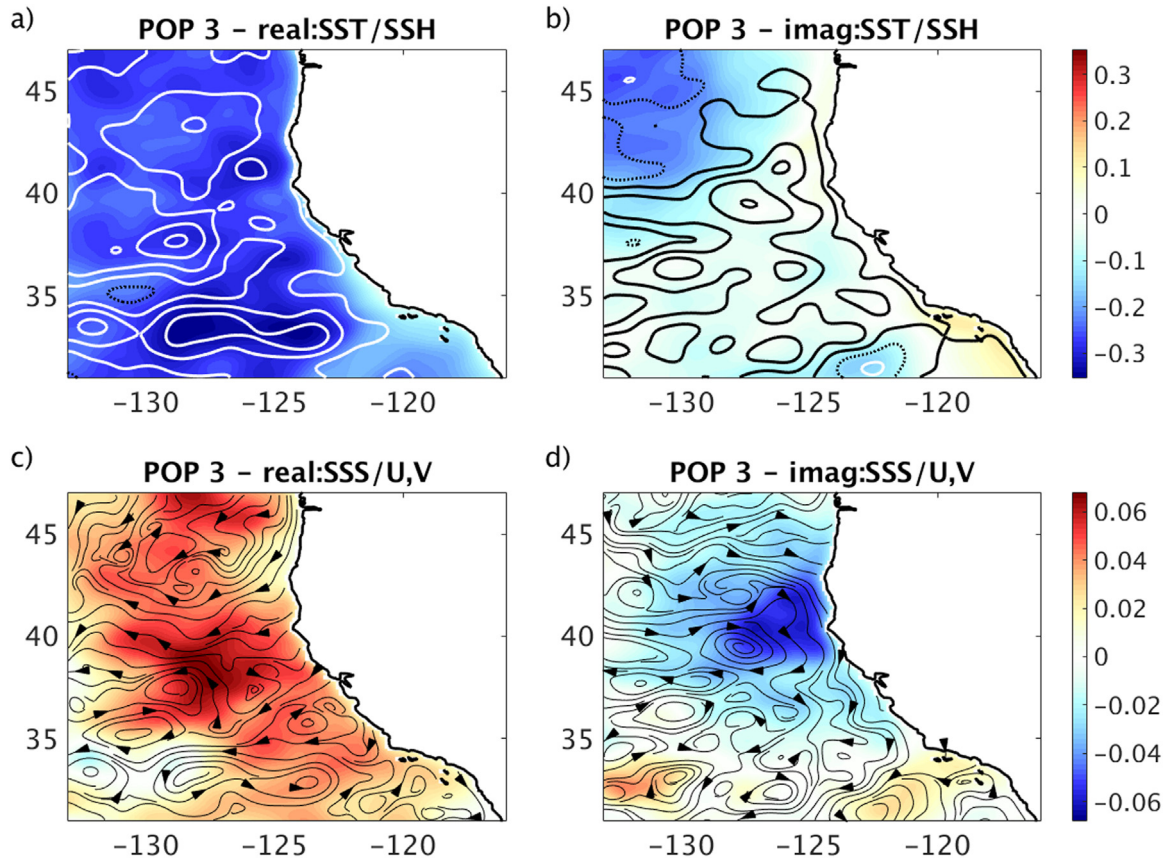
Fig. 6. The structure of the SST (color), SSH (contours), SSS (color) and surface circulation (streamlines) for the real and imaginary components of POP 3. The contour interval for SSH is 5×10^{-3} m, and black (white) contours indicate positive (negative) values. (For interpretation of the references to color in this figure legend, the reader is referred to the web version of this article.)
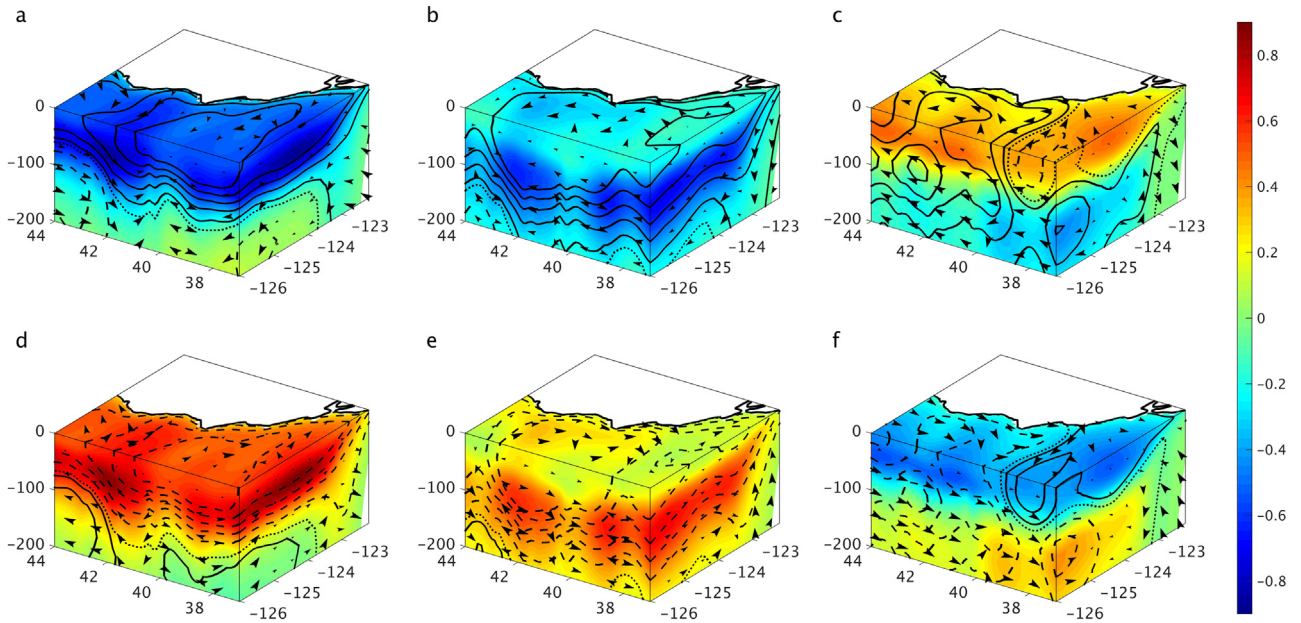
Fig. 7. A 3-dimensional view of the upper ocean structure of POP 3 off the central California coast. Temperature anomalies are shown in color, salinity anomalies as contours (negative values are dashed, and the contour interval is 0.02), and the 3-dimensional velocity anomalies as arrows. The size of the arrow is indicative of the relative magnitude of the velocity, and the vertical velocity component is scaled by 10^5 for ease of viewing. Panels (a) to (f) show the time evolution of the oscillatory component of POP 3 separated by intervals of 1/6 of a period (~ 1.6 years). (For interpretation of the references to color in this figure legend, the reader is referred to the web version of this article.)

in vertical velocity are confined to the coast (Fig. 8d) where upwelling (downwelling) anomalies are associated with cooler (warmer) SST and more (less) saline surface waters. The periods of anomalous upwelling and downwelling near the coast are also evident in the vertical sections of Fig. 7 near 36 °N. Fig. 7d shows the structure of the upper ocean anomalies in temperature, salinity and velocity during peak surface warming and freshening. At this time the thermocline is deeper than normal (cf Fig. 8a), and as the warm/fresh anomalies subside, the thermocline shallows and the equatorward California Current gains strength (Figs. 7e and f), and coastal upwelling is intensified (Fig. 8d).

4.2. Stochastic forcing of the POPs

According to the hypothesis underlying (1), the POPs are stochastically forced by the noise ξdt. As noted in Appendix C, the stochastic forcing can be estimated from $d\mathbf{u} - \widetilde{\mathbf{A}}\mathbf{u}$. Fig. 9 shows the surface variance of the stochastic forcing of δx mapped back into physical space (cf (1)). It is important to realize that even though the hypothesis behind (1) calls for forcing that is white in time, this does not preclude the stochastic forcing having spatial structure, which is apparent in Fig. 9. The forcing variance in SST is generally largest offshore and close to the coast with maximum values $\sim 1.5 \times 10^{-3}C$ day^{-1}. SSS forcing is most pronounced along the coast of northern California, Oregon and Washington ($\sim 5 \times 10^{-4}$psu day^{-1}). Interestingly the surface velocity forcing has largest amplitude in a region offshore and downstream of Cape Mendocino where eddy kinetic energy is generally elevated in altimeter and drifter observations (Kelly et al., 1998) and in the 4D-Var analyses (N16). There is also a narrow band of elevated surface velocity forcing variance spanning the CCS poleward of Cape Mendocino. The variance patterns in SST, SSS and velocity are coherent over the upper $200 - 300$m of the water column (not shown), while SSH forcing is relatively incoherent (Fig. 9a).

By definition, white noise forcing contains equal energy at all frequencies, although in this case the highest frequency possible will be πmonths^{-1}. It is therefore of interest to quantify the expected response of the system to forcing at different frequencies. With this in mind, consider the reduced rank approximation of (1) given by Eq. (B.5):

$$d\mathbf{u} = \widetilde{\mathbf{A}}\mathbf{u}dt + \widetilde{\xi}dt. \tag{3}$$

Suppose that the stochastic forcing $\widetilde{\xi}dt$ in (3) is replaced by a harmonic forcing of the form $\mathbf{h}e^{i\omega t}dt$, where ω is the forcing frequency and $\mathbf{Rh}$ (where $\mathbf{R}$ is the matrix of 3D EOFs) describes the 3D structure of the forcing, which for now is assumed to be arbitrary. Since all of the POPs of $\widetilde{\mathbf{M}}$ decay exponentially in time, then after a sufficiently long time interval the solution of (3) is given by $\mathbf{u}(t) = e^{i\omega t}(i\omega\mathbf{I} - \widetilde{\mathbf{A}})^{-1}\mathbf{h}$. The ratio of the system response to the forcing is given by $\| \mathbf{u}(t) \|/\| e^{i\omega t}\mathbf{h} \| \leq \| \mathcal{R}(\omega) \|$ where $\|\cdot\|$ denotes the L2-norm which is equivalent to the energy density norm for the EOF basis functions used here, and $\mathcal{R}(\omega) = (i\omega\mathbf{I} - \widetilde{\mathbf{A}})^{-1}$ is the resolvent matrix. The L2-norm of the resolvent $\| \mathcal{R}(\omega) \|$ is given by the largest singular value of $(i\omega\mathbf{I} - \widetilde{\mathbf{A}})^{-1}$. Furthermore, the resolvent norm $\| \mathcal{R}(\omega) \| \propto 1/\text{dist}(\Lambda, \omega)$, where $\text{dist}(\Lambda, \omega)$ is the distance function, and represents the *shortest* distance (in the complex plane) between the eigenspectrum of $\widetilde{\mathbf{A}}$ denoted Λ, and the forcing frequency $i\omega$. Fig. 10 shows $\| \mathcal{R}(\omega) \|$ vs ω, and indicates that the maximum response occurs at a forcing frequency centered on 9.7 years corresponding to the period of POP 3 (see Table 2). This is consistent with the distance function since the eigenfrequency λ_3 of POP 3 is much closer to the forcing frequency $i\omega$ than that of POP 4, which recall has a similar period but is damped very quickly.

In contrast, Fig. 10 also shows the resolvent norm of a LIM constructed from a non-data assimilative run of the model using the same prior forcing and open boundary conditions, and computed in exactly the same way as the LIM derived from the 4D-Var analyses. In this case the resonant peak near 10 years is absent, indicating that POP 3 is present *only* in the LIM derived from the 4D-Var analyses, and that the POPs are not merely mirroring the low frequency response of the model to surface forcing.

Based on Fig. 10, we expect *a priori* that the response of the CCS circulation to white noise forcing will be dominated by the decadal variability associated with POP 3. With this in mind, Fig. 11 shows the amplitude a_3 of POP 3 over the period 1981–2010. Recall that the natural tendency for POP 3 will be to decay in time. However, the decadal component of the stochastic forcing continually excites POP 3, so the variations in amplitude of $\mathbf{e}_3$ in Fig. 11 over time are controlled by the time variations of the stochastic forcing. This can be further
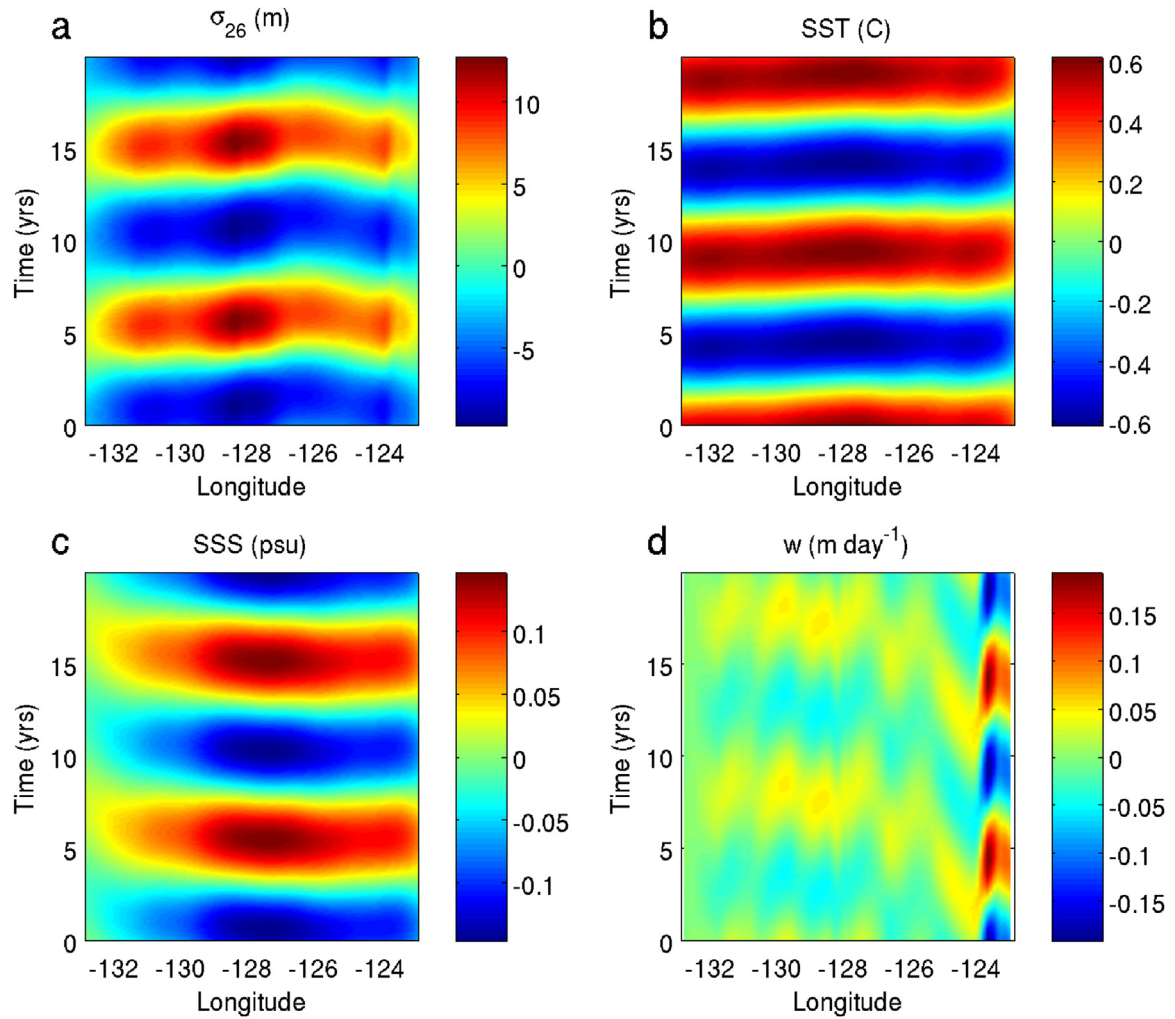
Fig. 8. Hovmoller diagrams of anomalies in (a) thermocline depth, (b) SST, (c) SSS and (d) w at 40 m at 38 °N for POP 3 over a 20 year period. The decaying component of the POP has been suppressed so as to highlight the oscillatory component. Positive (negative) thermocline depth anomalies correspond to a shallower (deeper) thermocline.

illustrated by considering the projection of POP 3 onto the 3D EOFs. Table 2 indicates that EOFs $\mathbf{r}_1$ and $\mathbf{r}_2$ project considerably onto each POP, particularly POP 3. Fig. 12a shows a phase plot of the amplitude of $\mathbf{r}_1$ and $\mathbf{r}_2$ during two cycles of POP 3. The red ellipse represents the oscillatory component of POP 3 alone (as described by $Im(\lambda_3)$), and illustrates the relative contribution of these two EOFs to POP 3 over time. The time required to complete one orbit around the ellipse is 9.7 years. The blue curve shows how the decay in POP 3 over time is mirrored by the amplitudes of EOFs $\mathbf{r}_1$ and $\mathbf{r}_2$. The influence of the stochastic forcing in the $\mathbf{r}_1 - \mathbf{r}_2$ phase plane of POP 3 is shown in Fig. 12b. While the variations in EOF amplitudes are somewhat random, the tendency of the system response to follow the red ellipse in Fig. 12b that describes the oscillatory component of POP 3 is quite obvious. The circulation associated with the stochastically forced fluctuations in the amplitude of POP 3 are illustrated in Fig. 13 at 38 °N. Comparing Fig. 13 with Fig. 8 shows how the oscillation described by POP 3 is continually excited and modulated by the stochastic forcing.

Obvious candidates for the forcing of POP 3 are ENSO, the NPGO and the PDO which are all known to influence the CCS circulation, as discussed in Section 1. Fig. 14 shows wavelet power spectra of the MEI, NPGO index and PDO index during the period 1980–2010. The width of the peak in Fig. 10 indicates that forcing with a period in the range $\sim 8 - 12$ years will be effective at exciting $\mathbf{e}_3$. Fig. 14 shows that both the NPGO and PDO have significant power in this frequency band, particularly during the period 1990–2005 when the amplitude of $\mathbf{e}_3$ is relatively high (cf Figs. 11 and 13). Even though the PDO index does

not display a peak in power in the 8–12 year band like the NPGO index, it is important to realize that any power in this range can be amplified by POP 3 as shown in Fig. 10. ENSO, on the other hand, has a broad band of power between 3- and 5-year periods (Fig. 14a) that will be quite effective at exciting $\mathbf{e}_1$ and $\mathbf{e}_2$ which, recall have periods of 3.6 and 5.2 years respectively (Table 2), although these modes are damped within a couple of years, which explains the absence of a peak at these frequencies in Fig. 10.

To quantify the relative contribution of the PDO, NPGO and ENSO in exciting POP 3, a regression analysis was performed between each climate mode index in Section 3.2 and the amplitude of the component of stochastic forcing $f_3 = (\mathbf{e}_3^\dagger)^H (d\mathbf{u} - \widetilde{\mathbf{A}})$ that projects directly onto POP 3. To isolate the low frequency components, the time series of f_3 and each climate index were smoothed using a 5-year running mean prior to the regression analysis. For example, Fig. 15a shows the amplitude of the forcing of POP 3 in SST associated with a one standard deviation change in the amplitude of the PDO index. Also shown in Fig. 15a is the fraction of variance in POP 3 SST forcing that is directly explained by the PDO index. The POP forcing takes the form of a 3-dimensional, multivariate, time evolving field so references here to forcing by the PDO are interpreted as the projection of the regional expression of the basin-wide circulation anomalies associated with the PDO onto the POP forcing fields. With this in mind, Fig. 15a indicates that the positive phase of the PDO is associated with a positive forcing of SST, and up to $35 - 40\%$ of the POP 3 SST forcing can be explained by the PDO. Fig. 15b shows the same analysis for the NPGO. In general, the pattern
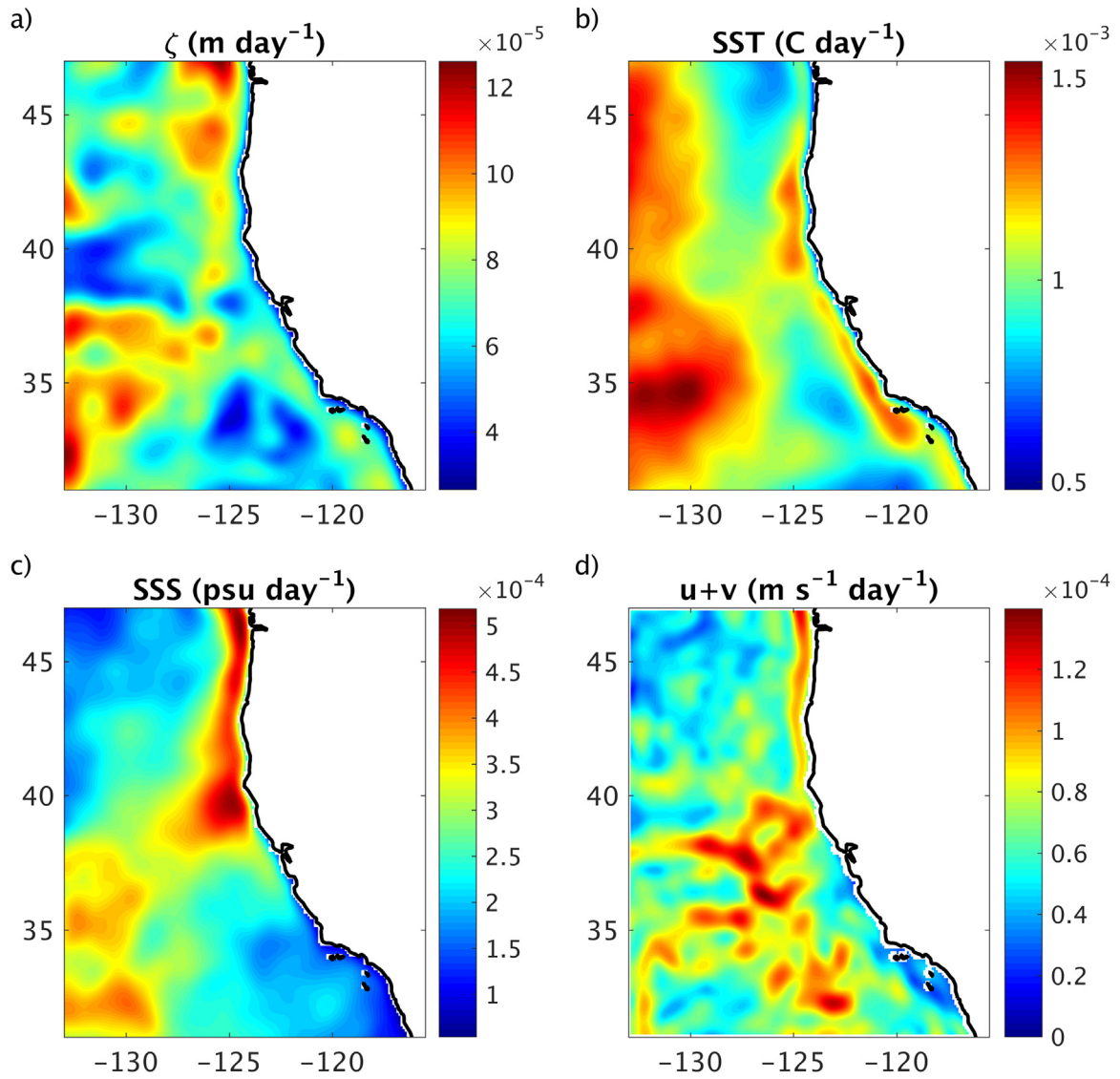
Fig. 9. Standard deviation of the stochastic forcing for (a) SSH, (b) SST, (c) SSS, (d) surface u and v combined.
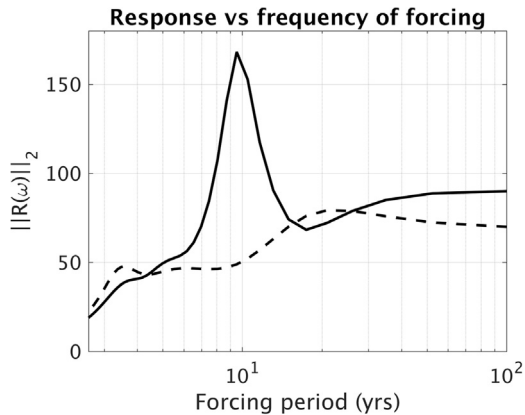

Fig. 10. The L2-norm of the resolvent $\mathscr{R}(\omega) = (i\omega \mathbf{I} - \widetilde{\mathbf{A}})^{-1}$ vs the period $2\pi/\omega$ of the forcing for a LIM computed from the 4D-Var analyses (solid line) and from a non-assimilative run of the model (dashed line).

Fig. 11. Time series of the real (solid line) and imaginary (dashed line) components of the amplitude of POP 3.

of SST forcing associated with NPGO is similar to that of the PDO, but in this case the positive phase of the NPGO is associated with a negative forcing of the POP 3 SST. Therefore, the opposite phases of the PDO and NPGO tend to reinforce the POP 3 circulation anomalies, although
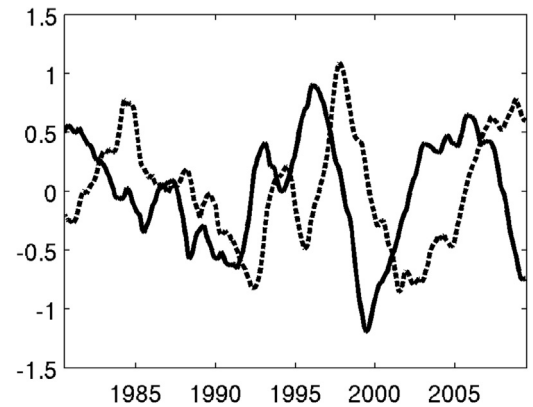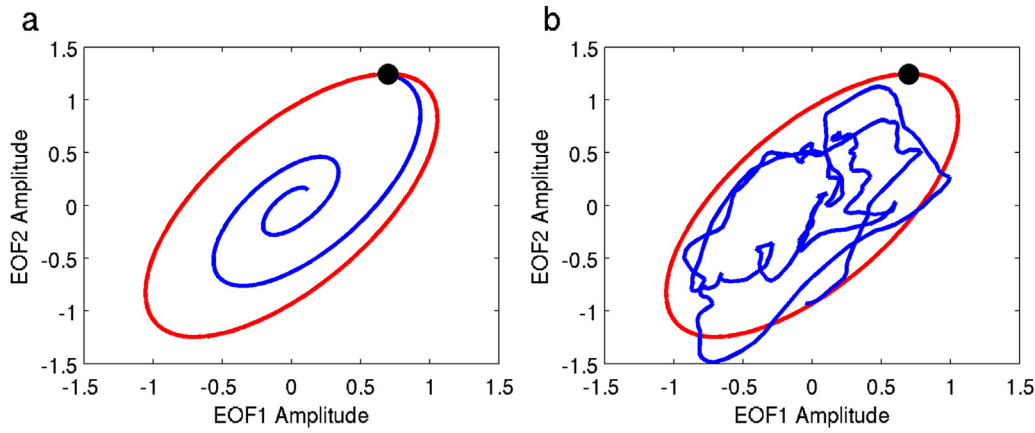
Fig. 15b shows that the amplitude and fraction of the $\mathbf{e}_3$ forcing accounted for by the NPGO is significantly lower than that of the PDO. The pattern of POP 3 SST forcing associated with the MEI is positive and similar to that of the PDO (not shown), since the correlation between the MEI and the PDO index is 0.6. However, the amplitude and fraction

Fig. 12. (a) A phase diagram of the amplitude of EOFs r_1 and r_2 for two cycles of POP e_3. The red curve shows the oscillatory component of e_3 and the blue curve includes the decaying component. The black circle indicates the starting point, and progression around the ellipse is clockwise. (b) A phase diagram of the amplitude of EOFs r_1 and r_2 based on the amplitude of e_3 during the period 1981–2010 (blue curve). The red curve is the same as that in (a). (For interpretation of the references to color in this figure legend, the reader is referred to the web version of this article.)
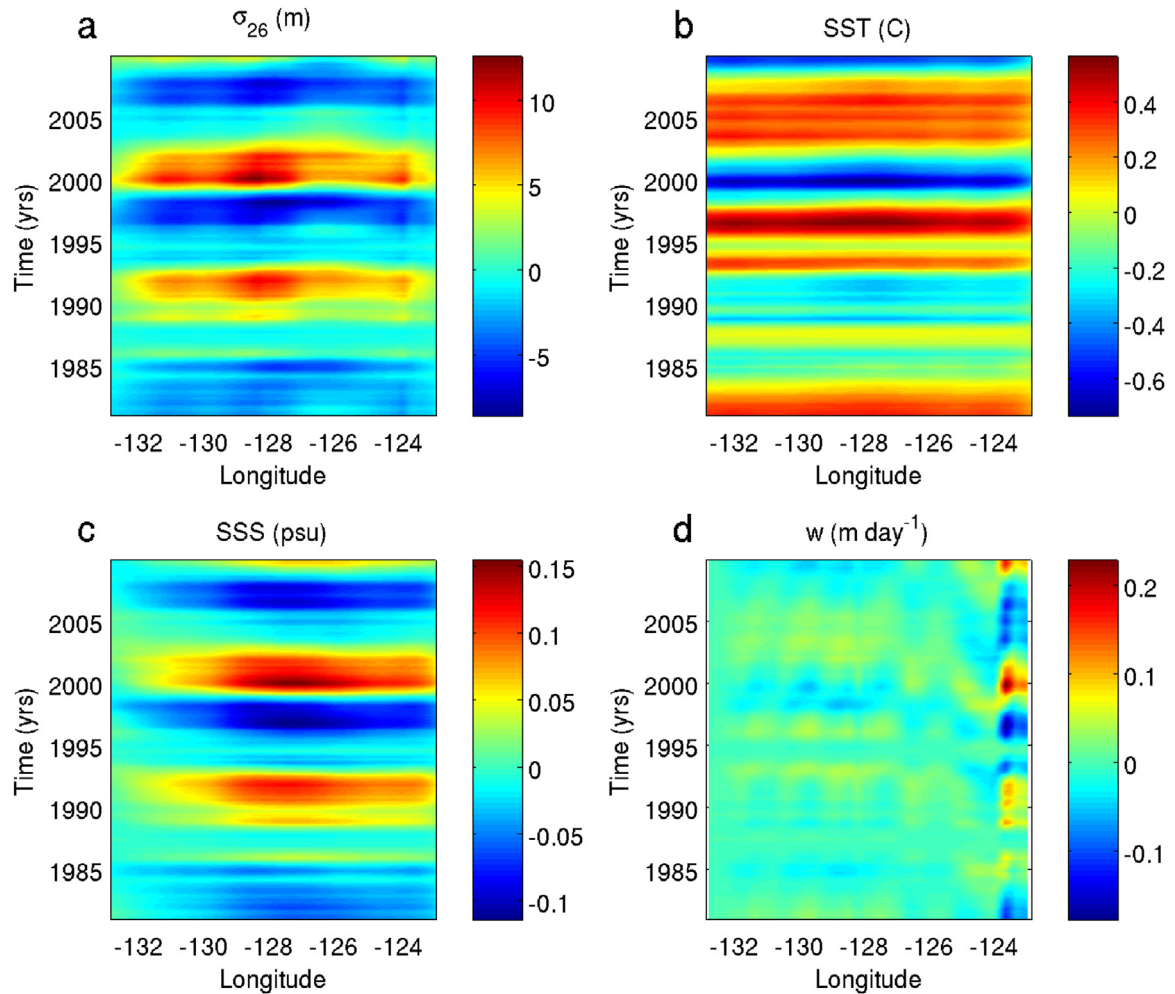

Fig. 13. Hovmoller diagrams of anomalies (a) thermocline depth, (b) SST, (c) SSS and (d) w at 40 m at 38 °N associated with the time varying amplitude of e_3 during the period 1981–2010. Positive (negative) thermocline depth anomalies correspond to a shallower (deeper) thermocline.

of variance explained by the MEI POP 3 forcing is similar to that of the NPGO. These same relationships between each climate index and the forcing of POP 3 apply to other state variables also, and extend well below the surface. For example, Fig. 15c shows the amplitude of POP 3 temperature forcing associated with the PDO along a vertical section at 38 °N. The forcing changes sign at the depth of the thermocline, and the variance explained remains high throughout the water column. Even though Fig. 14 indicates that the NPGO has more power at decadal periods than the PDO and MEI, the spatial structure of the forcing is

also very important (Farrell and Ioannou, 1996; Chhak et al., 2009a, 2009b). This can be quantified in terms of the stochastic optimals of (1) (Kleeman and Moore, 1997), but this is beyond the scope of the present paper.

Fig. 15d shows power spectra of the amplitude of the POP 3 forcing showing that it is elevated at frequencies close to those where the PDO and NPGO index have elevated power (Fig. 14). Hence, the POP 3 can very effectively resonate in response to circulation anomalies induced by the PDO, NPGO and to some degree by ENSO, even though the

a)

b)

c)
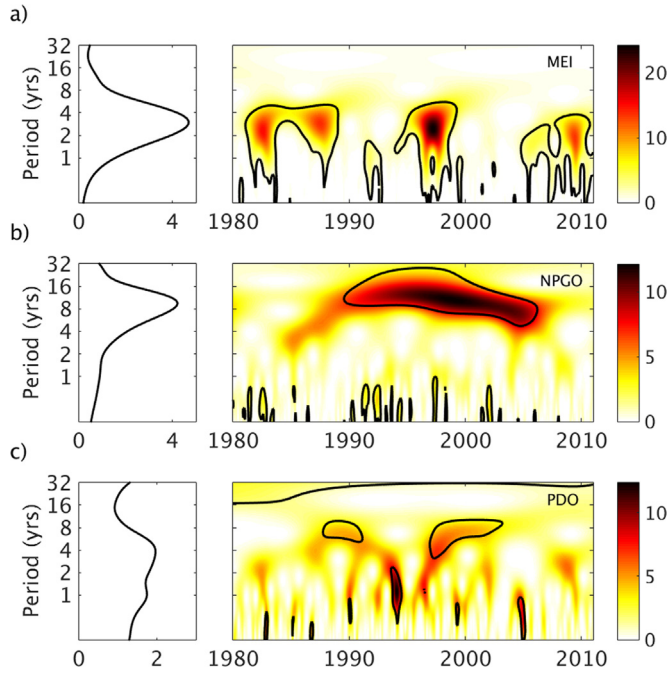
Fig. 14. Wavelet analyses of the MEI, NPGO index and PDO index for the period 1980–2010. In each case a Paul wavelet was used to provide good resolution in time. The regions enclosed by bold contours are significant at the 95% level. While each index time series spans a longer period than the 4D-Var analyses, only the portion of the wavelet spectra for the period 1980–2010 is shown here. The power averaged over time at each frequency is also shown to the left of each wavelet plot, and is an average over the full duration of each time series.

power at decadal periods in the MEI is relatively low (Fig. 14a).

5. Decadal variability in coastal upwelling

Using the same 4D-Var analyses, Jacox et al. (2014) hereafter J14 have documented low frequency variability in coastal upwelling along the central and northern California coast that is apparently correlated with ENSO, PDO and NPGO. Fig. 16 shows a time series of w averaged over the central California region indicated in Fig. 1 that is associated with the leading EOF of w at 40 m depth and the PC time series computed by J14. The PC reported by J14 also has an upward linear trend over the same period. However, to be consistent with the LIM (which recall is constructed from detrended PC time series), the linear trend was been removed from the time series shown in Fig. 16. When the time series is positive (negative), upwelling is enhanced (suppressed) along the entire central California coast extending 50 km off-shore, while between 50 and 200 km, upwelling is suppressed (enhanced).

Much of the variability in coastal upwelling documented by J14 is captured by a combination of POPs e_1, e_2 and e_3 as indicated in Fig. 16 which also shows w associated with the superposition of these three modes averaged over the same region shown in Fig. 1. The correlation between the time series in Fig. 16 is 0.84. However, much of the variability in this region captured by the leading EOF of w computed by J14 can be explained by e_3, and the correlation between the time series of w due to e_3 alone with w from J14 is 0.6 (not shown). The influence of POP 3 on coastal upwelling is illustrated in Fig. 17 which shows the phase of w associated with POP 3 and indicated that w varies coherently along the coast poleward of Point Conception (notice the phase at $\sim 40\,°N$ changes from near $+ 180°$ to $- 180°$ which are equivalent).

J14 note that the largest anomalies in coastal upwelling typically occur when the PDO and NPGO are out of phase, in agreement with the relative influence of the PDO and NPGO on POP 3 (Section 4.2). For example, during 1991–95, Fig. 16 indicates that total upwelling was suppressed in the central California region. Fig. 18 shows the

circulation anomalies in w, SST, SSS and thermocline depth during this period that are associated with the superposition of e_1, e_2 and e_3. The pattern of upwelling anomalies (Fig. 18a) is similar to that reported in J14. At the same time surface waters are warmer (Fig. 18c) and fresher (Fig. 18d) than normal over the whole domain, and the thermocline is deeper than normal (Fig. 18b). The vertical sections of temperature and salinity in Figs. 18e and f reveal that the surface anomalies are coherent over the upper 100–200 m.

Conversely, during the 1998–2002 time period total upwelling is weaker than normal along the northern California, Oregon and Washington coasts with generally colder, more saline surface waters across the entire region and a shallower than normal thermocline. Essentially, the reverse of that shown in Fig. 18.

Much of the variability in upwelling in Fig. 16 is associated with e_3 ($r = 0.6$). The relationship between w and other components of the circulation in the central California coastal region of Fig. 1 associated with e_3 is shown in Fig. 19 which demonstrates the phase relationship between different aspects of the coastal response. The phase of SST and w is consistent with upwelling induced cooling. SSS and thermocline depth on the other hand generally lag behind w by $\sim 1 - 2$ years.

The coastal upwelling changes documented by J14 therefore appear to be part of CCS-wide changes in the circulation that are captured in detail by the POPs. Much of this variability is captured by mode e_3 alone which, as shown in Section 4.2, is preferentially excited by the decadal components of the stochastic forcing acting on the system associated with the PDO, NPGO and ENSO. During the period 1990–2010, the PDO and NPGO were generally out of phase which had the effect of increasing the amplitude of the POP 3 circulation anomalies, which is very evident in Fig. 13. This also agrees with the analysis of Macias et al. (2012) who found that low-frequency variability in coastal upwelling along the central California coast is negatively (positively) correlated with the PDO (NPGO).

The general solution of the stochastic differential Eq. (1) is given in Appendix B by Eq. (B.2). The second term on the right hand side of (B.2) shows that the circulation at any time depends on the time history of the stochastic forcing and the stochastically integrated response of the POPs. Therefore, the response observed at any particular time will depend on forcing by the PDO and NPGO (and ENSO) over a range of times in the past. This can obscure the interpretation of the observed circulation, frustrating simple correlation analyses. For example, Eq. (B.2) shows that the response of the system due to stochastic forcing of e_3 is given by the integrated time history of the integrand $k(t') = e^{\widetilde{A}(t-t')}\xi_3(t')$, where ξ_3 is the component of stochastic forcing that projects onto e_3. Fig. 20 shows times series of the contribution of $k(t')$ to w for all times t' prior to Jan 1999 (Fig. 20a), the time of onset of suppressed upwelling, and Jan 2005 (Fig. 20b), the peak of a period of suppressed upwelling. Fig. 20 reveals that there are sizable contributions associated with the stochastic excitation of e_3 during the ~ 5 years preceding the circulation anomalies observed in Jan. 1999 and 2005, consistent with the long damping time of this mode (Table 2).

6. Summary and conclusions

Multivariate 3D EOFs were used to quantify the circulation variability captured by 4D-Var estimates of the CCS on various time scales over the period 1980–2010. The 3D EOFs uncover a far richer and more complex circulation environment than is revealed by more conventional 2D EOF analyses of surface fields alone. No single multivariate 3D EOF mode is able to isolate a single documented mode of climate variability, although variations in the amplitude of the leading EOF appear to correlate well with the observed downward trend in the PDO during the three decades considered.

Although many aspects of the 3D EOFs correlate well with ENSO, the NPGO and the PDO (which largely characterize climate variability in the North Pacific), a high level of correlation with the PDO and
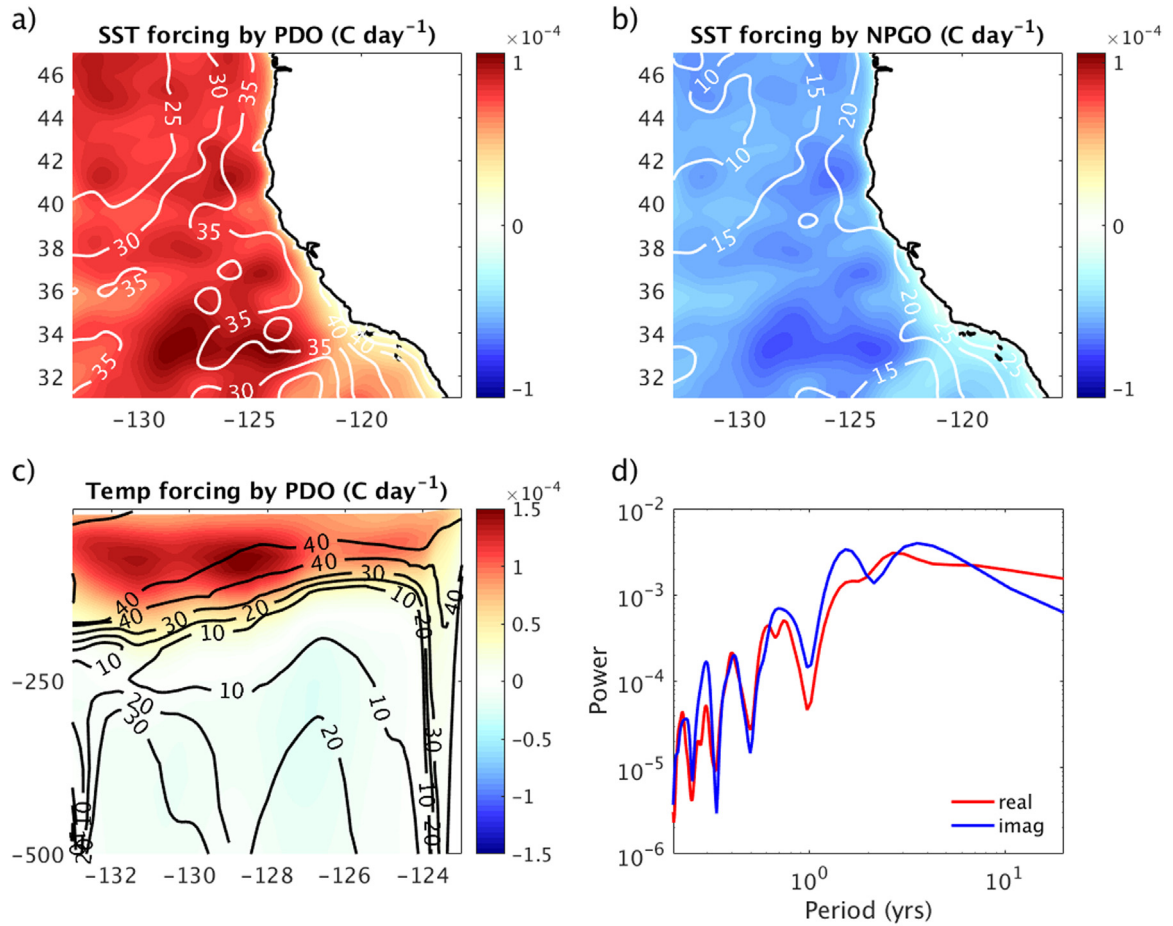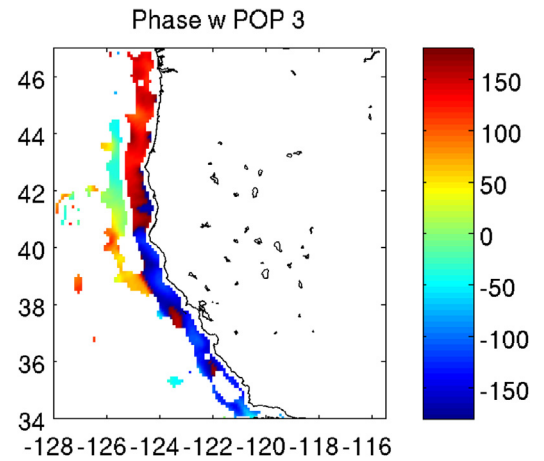
Fig. 15. Forcing of SST based on a linear regression between low-pass filtered forcing amplitude of POP3 and (a) the PDO index, (b) the NPGO index. The forcing shown results from a positive standard deviation change in the climate index. White contours indicate 100 times the coefficient of determination ($100 \times r^2$ values) and represent the percentage of variance of SST forcing of POP 3 explained by each index. (c) Same as (a) but showing a vertical section along 38 °N of temperature forcing by the PDO. (d) Power spectra of the real (red) and imaginary (blue) components of the POP 3 forcing amplitude. (For interpretation of the references to color in this figure legend, the reader is referred to the web version of this article.)
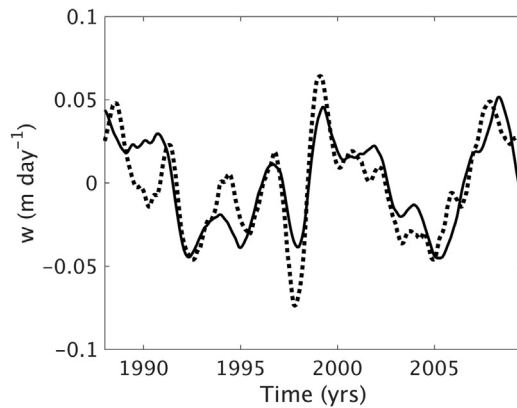
Fig. 16. The vertical velocity based on the first principal component time series and EOF *w* at 40 m depth over the region indicated in Fig. 1 from Jacox et al. (2014) after the linear trend has been removed (solid line). Time series of *w* associated with the superposition of e_1, e_2, and e_3 averaged over the same region (dashed line).

Fig. 17. The phase (degrees) of vertical velocity at 40 m associated with POP 3. The phase is given by $\tan^{-1}(Im(w)/Re(w))$. The phase in deep offshore regions where *w* is very small is not plotted.

NPGO is not necessarily to be expected since they are both defined in terms of EOFs of surface fields alone, with no recourse to subsurface information or ocean currents. To unravel the nature of the circulation variability in more detail, we computed the POPs of a LIM based on the PC time series of the leading 3D EOFs of the 4D-Var analyses.

The POPs reveal that the low frequency circulation anomalies can be described by three distinct modes of variability with periods ranging from ∼ 3.5 − 10 years. In addition, POP 3 which has the lowest

frequency can be resonantly excited with relative ease by virtue of its slow decay rate, and essentially any forcing in the system with a period of ∼ 8 − 12 years can be amplified by two orders of magnitude. Obvious potential sources of forcing in this frequency range are the regional expressions of the basin wide climate modes identified with the PDO, NPGO and ENSO, all of which possess power in the ∼ 8 − 12 years range. The POP 3 forcing identified here, by necessity, takes the form of
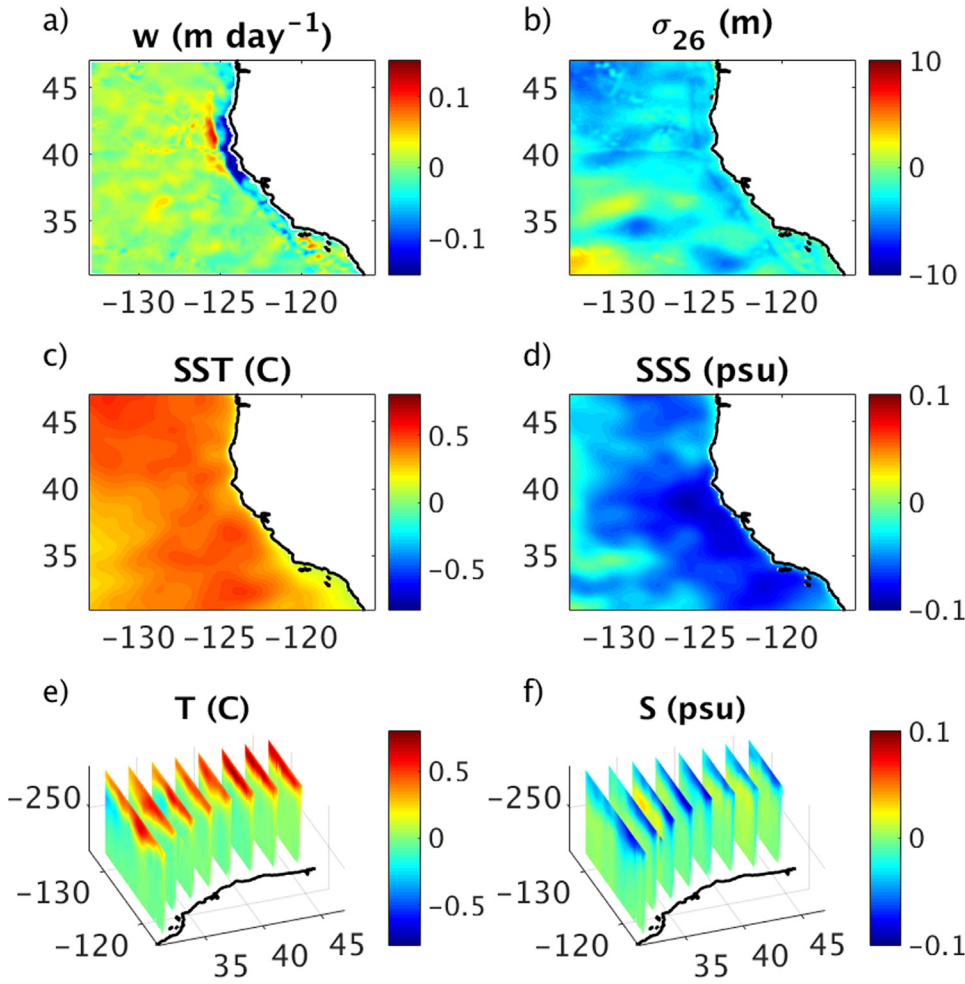
Fig. 18. Circulation anomalies associated with the superposition of e_1, e_2, and e_3 averaged over the period 1991–95 when upwelling is suppressed along the California coast (a) w at 40 m, (b) SST, (c) SSS and (d) thermocline depth. Also shown are vertical sections of (e) temperature and (f) salinity over the upper 500 m every 2° of latitude.
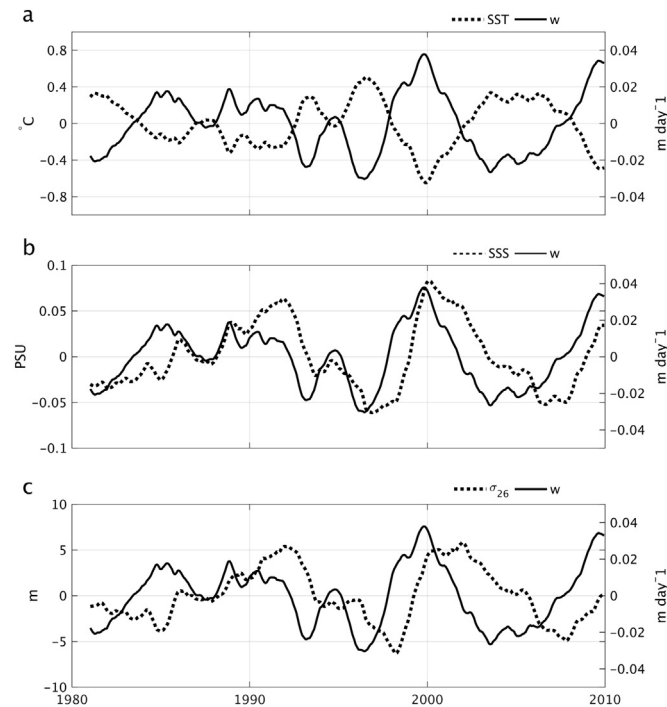

Fig. 19. Time series of anomalies in SST, thermocline depth, SSS and w at 40 m associated with e_3 averaged over the region shown in Fig. 1. Positive (negative) thermocline depth anomalies correspond to a shallower (deeper) thermocline.
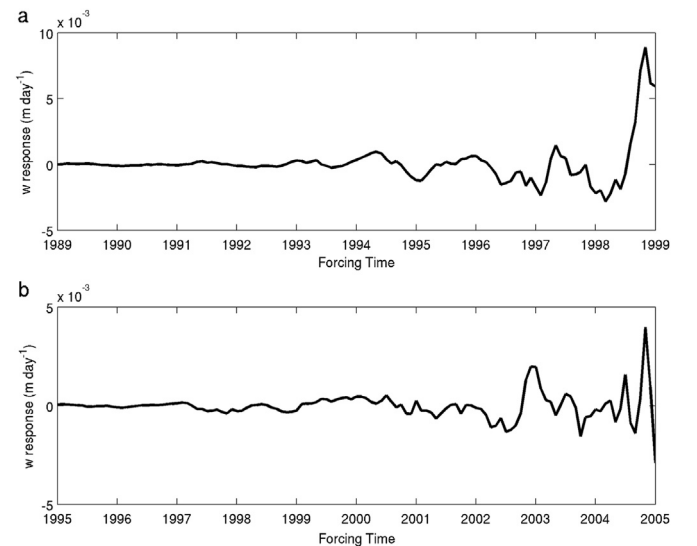

Fig. 20. Time series of the contribution to w from $k(t')$ of the stochastic forcing associated with e_3 through time to the response in w observed in (a) Jan 1999 and (b) Jan 2005.

3-dimensional, time-dependent fields. Therefore, when we refer to forcing by the PDO and NPGO we are referring to the regional components of basin scale 3D-circulation anomalies associated with the PDO and NPGO circulation changes, which in turn are associated with changes in the large-scale atmospheric circulation and ocean surface forcing as discussed in Section 1. Interestingly, the PDO and NPGO

forcing of POP 3 reinforce each other when the PDO and NPGO are out of phase, leading to extended periods of enhance or suppressed up-welling anomalies along the coast of central California, Oregon and Washington. This in turn is accompanied by low frequency anomalies in temperature, salinity and thermocline depth in line with those documented previously by J14.

The idea that much of the low frequency variability of the CCS is described by a resonantly forced mode of variability represents a new paradigm linking the basin scale climate modes and the coastal circulation, and suggests that in the CCS much of the circulation variability arises from an inherent, perhaps coastally trapped, mode of coastal variability that is resonantly forced by the regional expression of the basin scale climate modes. Therefore, while there have been several notable attempts to relate changes in the CCS circulation to the basin scale variability associated with the PDO and NPGO, the stochastically forced nature of the CCS variability will frustrate traditional attempts to understand the circulation using correlation analysis.

The true nature of the POPs identified here is not fully understood. It is possible that the POPs we have identified are simply inherent modes of oscillation of the particular model configuration used here (analogous to traditional basin modes of a bounded basin, Pedlosky (1979). However, this seems unlikely since a LIM derived from a non-data assimilative model run does not reproduce the same POPs (cf Fig. 10). The role played by the observations during data assimilation in controlling the POP amplitudes has been further explored by Moore et al. (2017) who have investigated the impact of the observing system

on various aspects of the circulation estimates used in the present analysis. Both satellite SST and SSH observations were found to play the largest role in capturing POP 3, although in situ measurements at ∼ 100 m depth were also found to be potentially important, since they are the only observations to provide information about the thermocline depth and upper ocean heat content. Nonetheless, since the mean circulation and bathymetry of the region is complex, further work is needed to identify the detailed nature of the POPs.

POPs 1, 2 and 3 are robust across a wide range of parameters which adds confidence to the findings of this study. While we have concentrated here primarily on the decadal POP, the POPs 1 and 2 with periods of 3.6 and 5.2 years are also of interest since they appear to capture CCS variability associated with ENSO (not shown). This will be the topic of a future study.

Finally we note that the memory imparted on the CCS circulation anomalies by the low frequency POPs identified here suggests that there may be potential to use the LIM to make seasonal predictions of the low frequency CCS circulation anomalies. C.3 (Fig. C.3) suggests that the LIM is able to hindcast the circulation anomalies for lead times up to 12 months, significantly beating persistence.

Appendix A

Computation of 3D multivariate EOFs

Following the notation used in N16, the ROMS state-vector is denoted by $\mathbf{x} = (T, S, u, v, \zeta)^T$ and comprises all grid point values of temperature T, salinity S, the two horizontal components of velocity (u,v), and the sea surface displacement, ζ. Here, we compute the EOFs of the multivariate covariance matrix:

$$\mathbf{C} = \frac{1}{n} \sum_{i=1}^{31} \sum_{j=1}^{12} (\mathbf{w}_{i,j} - \overline{\mathbf{w}}_j)(\mathbf{w}_{i,j} - \overline{\mathbf{w}}_j)^T \tag{A.1}$$

where $\mathbf{w}_{i,j} = \mathbf{W}^{\frac{1}{2}}\mathbf{x}_{i,j}$ and $\mathbf{x}_{i,j}$ is the monthly mean state-vector for month j, year i for the 31-year period 1980–2010 which yields a sample size $n = 372$; $\overline{\mathbf{w}}_j = \sum_{i=1}^{31} \mathbf{w}_{i,j}/31$ is the monthly mean climatology for month j computed from the 31-year sequence of analyses; and $\mathbf{W}^{\frac{1}{2}}$ is the diagonal matrix of weights applied to each state-vector element. Since the elements of $\mathbf{x}$ have different physical dimensions, the primary purpose of $\mathbf{W}^{\frac{1}{2}}$ is to transform $\mathbf{x}$ into the vector $\mathbf{w}$ in which all elements are appropriately rescaled to be dimensionless or to have the same units. By definition, the 3D multivariate EOFs are the eigenvectors of $\mathbf{C}$ such that $\mathbf{C}\mathbf{s}_k = \nu_k\mathbf{s}_k$. The EOFs $\mathbf{s}_k$ can be transformed back to familiar physical units according to $\mathbf{r}_k = \mathbf{W}^{-\frac{1}{2}}\mathbf{s}_k$, and the EOFs $\mathbf{r}_k$ are orthonormal with respect to $\mathbf{W}$ so that $\mathbf{r}_i^T\mathbf{W}\mathbf{r}_j = \delta_{i,j}$.

A.1. The Choice of $\mathbf{W}$

Several choices for the weight matrix $\mathbf{W}$ were considered. In the first case, denoted $\mathbf{W}_1$, the weight matrix $\mathbf{W}$ implicit in (A.1) was chosen so that the trace of the covariance matrix yields the perturbation energy per unit volume (hereafter referred to as the energy density) given by:

$$\mathscr{E}_{i,j} = (\mathbf{x}_{i,j} - \overline{\mathbf{x}}_j)^T\mathbf{W}_1(\mathbf{x}_{i,j} - \overline{\mathbf{x}}_j) = \frac{\rho_0 g}{2V} \int_{\lambda_w}^{\lambda_e} \int_{\phi_s}^{\phi_n} \Delta\zeta_{i,j}^2 \, a \cos\phi \, d\lambda d\phi + \frac{\rho_0}{2V} \int_{-H}^{\zeta_{i,j}} \int_{\lambda_w}^{\lambda_e} \int_{\phi_s}^{\phi_n} [\Delta u_{i,j}^2 + \Delta v_{i,j}^2 + (\alpha^2 \Delta T_{i,j}^2 + \beta^2 \Delta S_{i,j}^2)g^2/N^2] a \cos\phi \, d\lambda d\phi dz \tag{A.2}$$

where $\Delta T_{i,j}$, $\Delta S_{i,j}$, $\Delta u_{i,j}$, $\Delta v_{i,j}$ and $\Delta\zeta_{i,j}$ are respectively the temperature, salinity, zonal velocity, meridional velocity, and free surface height component of $(\mathbf{x}_{i,j} - \overline{\mathbf{x}}_j)$; (λ_w, λ_e) and (ϕ_s, ϕ_n) define the west-east longitudinal and south-north latitudinal extent of the model domain; $H(\lambda, \phi)$ is the ocean depth; α is the thermal expansion coefficient; β is the salinity contraction coefficient; N^2 is the squared Brunt-Väisälä frequency; V is the ocean volume of the domain; and all other symbols have their usual meaning. In the case of $\mathbf{W}_1$, representative values of α, β and N^2 were chosen corresponding to $\alpha = 1.6 \times 10^{-4}\text{K}^{-1}$, $\beta = 7.6 \times 10^{-4}$ and $N^2 = 10^{-5}\text{s}^{-2}$. From (A.2), $\text{Tr}(\mathbf{C}_1) = 1/n \sum_{i=1}^{31} \sum_{j=1}^{12} \mathscr{E}_{i,j}$ which is the total variance measured in terms of the energy density. Using this definition of $\mathbf{W}_1$, allowance is made for the difference in physical units of each state variable, and following North et al. (1982), each state variable is appropriately weighted by the volume of each model grid cell. The perturbation energy density $\mathscr{E}_{i,j}$ defined by (A.2) is considered to be an appropriate norm because of the obvious significance and fundamental importance of energy for describing the ocean circulation. A time series of $E_1 = (\mathbf{x}_{i,j} - \overline{\mathbf{x}}_j)^T\mathbf{W}_1(\mathbf{x}_{i,j} - \overline{\mathbf{x}}_j)$ is shown in Fig. A.1 and illustrates how the monthly mean energy density varies in time during WCRA31.

The second choice of $\mathbf{W}$, denoted $\mathbf{W}_2$, was also based on the energy norm (A.2) except in this case the spatially varying time mean values of α, β and N^2 were used. A time series of $E_2 = (\mathbf{x}_{i,j} - \overline{\mathbf{x}}_j)^T\mathbf{W}_2(\mathbf{x}_{i,j} - \overline{\mathbf{x}}_j)$ is also shown in Fig. A.1. While the amplitude of E_2 is smaller than E_1, the two time series are highly correlated ($r = 0.88$). The two additional choices of $\mathbf{W}$ considered were based on non-dimensionalizing the elements of $\mathbf{x}$ using
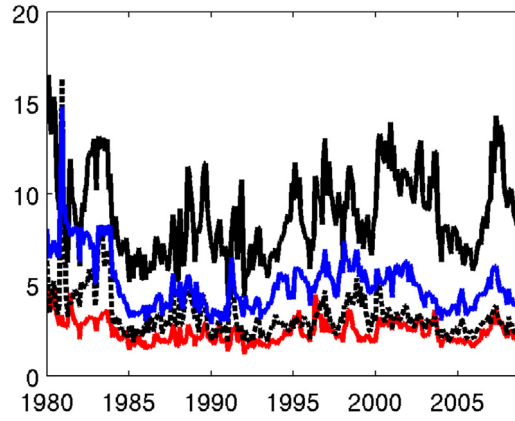
Fig. A.1. Times series of E_1 (solid black curve), E_2 (red curve), E_3 (dashed black curve) and E_4 (blue curve).

$\sigma_x^{-1} dV/V$ where σ_x is the standard deviation of each state-vector variable, and dV/V is the fractional volume of each grid cell. In the case of $\mathbf{W}_3^{\frac{1}{2}}$, a single value of σ_x based on the standard deviation computed from all grid points was used, while for $\mathbf{W}_4^{\frac{1}{2}}$ the σ_x were the standard deviations computed at each model grid point. Time series of $E_3 = (\mathbf{x}_{i,j} - \bar{\mathbf{x}}_j)^T \mathbf{W}_3 (\mathbf{x}_{i,j} - \bar{\mathbf{x}}_j)$ and $E_4 = (\mathbf{x}_{i,j} - \bar{\mathbf{x}}_j)^T \mathbf{W}_4 (\mathbf{x}_{i,j} - \bar{\mathbf{x}}_j)$ are shown in Fig. A.1. The correlation between E_3 and E_4 is 0.84 indicating that the variability captured by either choice of $\mathbf{W}_3$ and $\mathbf{W}_4$ is similar. The correlations between the energy-based time series E_1 and E_2 and the standard deviation-based time series E_3 and E_4 are ~ 0.5. These correlations increase to $\sim 0.7 - 0.8$ if a 12-month running mean is applied to each time series, which indicates that each norm is capturing similar low frequency variability.

The 3D multivariate EOFs are by definition the eigenvectors of $\mathbf{C}$ such that $\mathbf{C}\mathbf{s}_k = \nu_k \mathbf{s}_k$. In the case of $\mathbf{C}_1$ and $\mathbf{C}_2$, all of the elements of $\mathbf{s}_k$ have the units of $(\mathrm{Jm}^{-3})^{\frac{1}{2}}$, while in the case of $\mathbf{C}_3$ and $\mathbf{C}_4$ the $\mathbf{s}_k$ are dimensionless.

By and large, the leading EOFs that emerge are relatively insensitive to the choice of $\mathbf{W}$. The first two EOFs, $\mathbf{r}_1$ and $\mathbf{r}_2$, occupy the same position within the spectrum in each case, while the higher order EOFs some times trade positions. In the POP analysis of Section 4, we consider the leading 10 EOFs. The fraction of $\mathrm{Tr}(\mathbf{C})$ accounted for by the leading 10 EOFs is highest in the case of $\mathbf{W}_1$ (57%) (compared to 50% for $\mathbf{W}_2$, 46% for $\mathbf{W}_3$ and 39% for $\mathbf{W}_4$), so this is the case that we focus on here.

A.2. The Lanczos algorithm

The eigenvectors of the covariance matrix $\mathbf{C}$ defined by (A.1) were computed iteratively using the Lanczos algorithm (Golub and Van Loan, 1989). The basis of the Lanczos algorithm is a reduced rank factorization of $\mathbf{C}$ so that:

$$\mathbf{C} \simeq \mathbf{V}_m \mathbf{T}_m \mathbf{V}_m^T \tag{A.3}$$

where m refers to the number of iterations; $\mathbf{V}_m$ is a matrix where each of the m columns is a Lanczos vector $\mathbf{v}$; and $\mathbf{T}_m$ is an $m \times m$ tridiagonal matrix. The Lanczos vectors are orthonormal so that $\mathbf{V}_m^T \mathbf{V}_m = \mathbf{I}_m$, and satisfy the Lanczos recursion relation:

$$\mathbf{C}\mathbf{v}_i = \gamma_i \mathbf{v}_{i+1} + \delta_i \mathbf{v}_i + \gamma_{i-1} \mathbf{v}_{i-1} \tag{A.4}$$

where $\delta_i = \mathbf{v}_i^T \mathbf{C}\mathbf{v}_i$ are the elements of the leading diagonal of $\mathbf{T}_m$ and $\gamma_i = (\mathbf{a}_i^T \mathbf{a}_i)^{\frac{1}{2}}$ are the off-diagonal elements where $\mathbf{a}_i = \mathbf{C}\mathbf{v}_i - \delta_i \mathbf{v}_i - \gamma_{i-1}\mathbf{v}_{i-1}$. Each iterate of the Lanczos algorithm yields an additional Lanczos vector according to the Lanczos recursion relation (A.4). The algorithm is initialized by choosing $\mathbf{v}_1$ to be a random vector, and in the calculations presented here, the Lanczos vectors were reorthogonalized at the end of every iteration following Fisher (1997, pers. comm.).

The eigen pairs of the reduced rank approximation of $\mathbf{C}$ in (A.3) are given by $\mathbf{V}_m \mathbf{T}_m \mathbf{V}_m^T \boldsymbol{\psi}_k = \mu_k \boldsymbol{\psi}_k$, and $(\mu_k, \boldsymbol{\psi}_k) \to (\nu_k, \mathbf{s}_k)$, the true eigen pairs of $\mathbf{C}$, as m approaches the dimension of $\mathbf{C}$. The problem of identifying the eigen pairs of (A.3) reduces to finding the eigenvalues and eigenvectors of the much smaller $m \times m$ matrix $\mathbf{T}_m$ since $\mathbf{C}$ and $\mathbf{T}_m$ have the same eigenvalues in the limit as m approaches the dimension of $\mathbf{C}$. Specifically, $\mathbf{T}_m \mathbf{y}_k = \mu_k \mathbf{y}_k$, and the approximate eigenvectors of $\mathbf{C}$ are given by $\boldsymbol{\psi}_k = \mathbf{V}_m \mathbf{y}_k$. As the number of iterations m increases, the eigen pairs $(\mu_k, \boldsymbol{\psi}_k)$ become progressively better approximations of the true eigen pairs $(\nu_k, \mathbf{s}_k)$. The error in μ_k and $\boldsymbol{\psi}_k$ can be formally quantified according to $\epsilon_k = \| \gamma_k \mathbf{v}_{m+1}(\mathbf{e}_m^T \boldsymbol{\psi}_k) \| / \mu_1$ which follows directly from (A.4), where $\mathbf{e}_m$ is the unit vector with all zero elements except the mth element, and μ_1 is the largest eigenvalue of $\mathbf{T}_m$.

To illustrate, Fig. A.2a shows estimates of the leading eigenvalues of $\mathbf{C}_1$ based on $\mathbf{W}_1$ computed using $m = 60$ iterations. The formal error estimates ϵ_k are shown in Fig. A.2b and indicate that $\epsilon_k < 10^{-10}$ for the leading 20 eigenvectors, which lends confidence to the reliability of the EOFs presented in Section 3. Figs A.2a and b also show the leading eigenvalues and error estimates for the case $m = 120$ to illustrate how the estimates of μ_k are refined by further Lanczos iterates. The leading 30 or so eigenvalues and eigenvectors (not shown) change very little (Fig. A.2a) while the accuracy of the eigen spectrum improves substantially in the range $k = 20 - 50$ (Fig. A.2b).

Fig. A.2c shows the cumulative percent variance $100 \sum_{i=1}^{M} \mu_i / \mathrm{Tr}(\mathbf{C}_1)$ (i.e. perturbation energy density) versus M explained by the leading $M = 1, \ldots, 60$ eigenvectors, which as expected slowly asymptotes toward a value of 100%. As the number of iterations increases, the accuracy of the trailing eigenvalues increases, and the cumulative variance explained moves closer to 100% as illustrated in Fig. A.2c which also shows the cumulative variance for the case where $m = 120$.
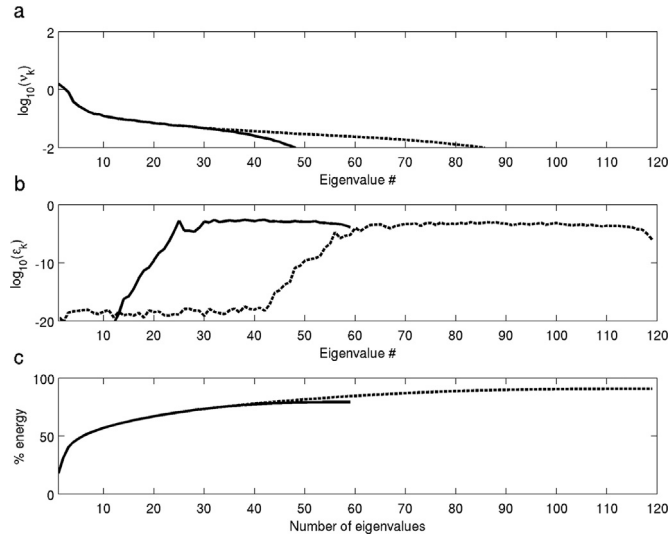
Fig. A.2. (a) Estimates of the leading eigenvalues of $\mathbf{C}_I$ computed using the Lanczos algorithm for $m = 60$ iterates (solid curve) and $m = 120$ iterates (dashed curve). (b) Formal estimates of the error ϵ associated with each eigen pair for $m = 60$ (solid curve) and $m = 120$ (dashed curve). (c) The fraction of variance $\mathrm{Tr}(\mathbf{C}_I)$ explained by the first M eigenvalues versus M for the case $m = 60$ (solid curve) and $m = 120$ (dashed curve).

Appendix B

Linear inverse model computation

Following the notation introduced in Appendix A, let $\overline{\mathbf{x}}$ represent the time mean state vector, and $\delta\mathbf{x} = \mathbf{x} - \overline{\mathbf{x}}$ denote departures of $\mathbf{x}$ from the mean. If $\delta\mathbf{x}$ is in statistical equilibrium, the hypothesis set forth in linear inverse modeling is that $\delta\mathbf{x}$ can be modeled as a stable, stochastically forced, linear system (i.e. as a first-order autoregressive or Markov process), so that:

$$d\delta\mathbf{x} = \mathbf{A}\delta\mathbf{x}dt + \boldsymbol{\xi}dt \tag{B.1}$$

where $\mathbf{A}$ is the dynamical system matrix that describes the time rate of change of $\delta\mathbf{x}$, and $\boldsymbol{\xi}dt$ is a white noise (in time) stochastic forcing. If $\mathbf{A}$ is time invariant, the solution of (B.1) is given by:

$$\delta\mathbf{x}(t + \tau) = e^{\mathbf{A}\tau}\delta\mathbf{x}(t) + \int_{t}^{t+\tau} e^{\mathbf{A}(t-t')}\boldsymbol{\xi}(t')dt'. \tag{B.2}$$

The eigenvectors of $\mathbf{A}$ (or equivalently $e^{\mathbf{A}\tau}$) are often referred to as normal modes. The leading normal modes can be computed iteratively in ROMS using the tangent linear model linearized about an appropriate basic state circulation (Moore et al., 2004). However, for large dimensional systems, like that considered here, such calculations are computationally and technically very challenging. Instead, the leading normal modes can be approximated using a linear inverse model (LIM). Following von Storch et al. (1995), consider the expected value of (B.2) after both sides are right multiplied by $\mathbf{W}\delta\mathbf{x}^T(t)$ (where $\mathbf{W}$ is the weight matrix in (A.1)) so that:

$$\langle\delta\mathbf{x}(t + \tau)\mathbf{W}\delta\mathbf{x}^T(t)\rangle = e^{\mathbf{A}\tau}\langle\delta\mathbf{x}(t)\mathbf{W}\delta\mathbf{x}^T(t)\rangle + \langle\int_{t}^{t+\tau} e^{\mathbf{A}(t-t')}\boldsymbol{\xi}(t')dt'\mathbf{W}\delta\mathbf{x}^T(t)\rangle. \tag{B.3}$$

Since $\delta\mathbf{x}(t)$ is statistically independent of the stochastic forcing $\boldsymbol{\xi}$ for $t' \geq t$ (i.e. $\delta\mathbf{x}$ is a non-anticipating function), then for white noise the last term in (B.3) is identically zero (see Gardiner, 1985, p90, Section 4.2.6(e)) which leads to:

$$\mathbf{M} = e^{\mathbf{A}\tau} = \mathbf{C}(t + \tau)\mathbf{C}(t)^{-1} \tag{B.4}$$

where $\mathbf{C}(t) = \langle\delta\mathbf{x}(t)\mathbf{W}\delta\mathbf{x}^T(t)\rangle$ is the zero-lag covariance matrix, and $\mathbf{C}(t + \tau) = \langle\delta\mathbf{x}(t + \tau)\mathbf{W}\delta\mathbf{x}^T(t)\rangle$. Eq. (B.4) shows that the normal modes can be approximated as the eigenvectors of $\mathbf{M}$ computed from the covariance matrix $\mathbf{C}(t)$ and $\mathbf{C}(t + \tau)$. However, (B.4) can still be difficult to use in practice since $\mathbf{C}(t)^{-1}$ will be difficult to evaluate for a large dimensional system. Following von Storch et al. (1995) and Penland and Sardeshmukh (1995), the dimension of the problem can be greatly reduced by recasting (B.1) in terms of the EOFs of $\mathbf{C}(t)$. Following Appendix A, the departures of the state vector from the mean can be expressed as $\delta\mathbf{x}(t) = \mathbf{R}\mathbf{u}(t)$ where $\mathbf{R}$ is the matrix of 3D EOFs $\mathbf{r}_i$ and $\mathbf{u}(t) = (u_i(t))$ is the vector of principal component time series. In this case (B.1) becomes:

$$d\mathbf{u} = \widetilde{\mathbf{A}}\mathbf{u}dt + \widetilde{\boldsymbol{\xi}}dt \tag{B.5}$$

where $\widetilde{\mathbf{A}} = \mathbf{R}^T\mathbf{W}^{\frac{1}{2}}(\mathbf{W}^{\frac{1}{2}}\mathbf{A}\mathbf{W}^{-\frac{1}{2}})\mathbf{W}^{\frac{1}{2}}\mathbf{R}$ which has the same eigenvalues as $\mathbf{A}$. The normal modes of (B.5) can be approximated as before in terms of the zero-lag covariance matrix as the eigenvectors of:

$$\widetilde{\mathbf{M}} = \boldsymbol{\Phi}(t + \tau)\boldsymbol{\Phi}(t)^{-1} \tag{B.6}$$

where $\boldsymbol{\Phi}(t) = \langle\mathbf{u}(t)\mathbf{u}^T(t)\rangle$ and $\boldsymbol{\Phi}(t + \tau) = \langle\mathbf{u}(t + \tau)\mathbf{u}^T(t)\rangle$. By virtue of the orthogonality of the PC time series, $\boldsymbol{\Phi}(t)^{-1}$ reduces to a diagonal matrix and the dimension of the problem can be greatly reduced by retaining only the leading 3D EOFs of $\mathbf{C}(t)$.

Appendix C

Tests of the linear inverse model (LIM) assumptions

As discussed by Penland and Sardeshmukh (1995), there are a number of fairly stringent tests that can be performed in order to test the hypothesis underlying (B.1), namely that the circulation anomalies $\delta \mathbf{x}$ can be modeled as a linear, stochastically forced system. This is equivalent to assuming that the circulation is described by an order one Markov process, often also referred to as a lag-1 autoregressive process (AR(1)). This appendix documents the results of various tests that were performed to test the validity of this hypothesis. In all of the calculations presented here, a linear trend was removed from each PC time series $\mathbf{u}(t)$.

C.1. Sensitivity of POP frequencies to time-lag τ and number of EOFs

We will first consider the sensitivity of the eigenvalues λ of the LIM to the choice of time-lag, τ, and the number EOFs retained, N. Fig. C.1a shows the spectrum of the eigenvalues of $\widetilde{\mathbf{M}}$ in (B.6), i.e. the POP frequencies, for a LIM using $N = 14$ EOFs. The lag-time τ varies between 6 and 20 months, and the eigen frequencies for each τ are shown in different colors, changing gradually from red for $\tau = 6$ to blue for $\tau = 20$. Three distinct branches of eigen frequencies are apparent that are labeled POP 2, POP 3 and POP 5 corresponding to the POPs identified in Table 2. Fig. C.1a indicates that the period ($2\pi/Im(\lambda)$) of POPs 2 and 3 is relatively insensitive to τ, while the decay time ($1/Re(\lambda)$) increases with τ (i.e. the POPs become increasing more stable). Both the period and decay time of POP 5 are sensitive to τ, and this mode is not reliable until its period approaches ~ 25 years. Fig. C.1b shows the same information for the LIM configuration used in Sections 4 and 5 where the PC time series were smoothed using a 12 month running mean prior to constructing the LIM. In this case, $N = 10$ and four distinct branches of solutions emerge corresponding to POPs 1, 2, 3 and 5 identified in Table 2 for the case $\tau = 6$.

The sensitivity of the POP 3 period and decay time to the number of EOFs, N, used in the LIM is shown in Fig. C.1c for the case using unsmoothed PC time series and $\tau = 12$, Both the period and decay rate are relatively insensitive to the choice of N. The decay rate of POP 3 is more sensitive to N when the PC time series are smoothed using a 12 month running mean as shown in Fig. C.1d. The dependence of the period and decay time on the averaging period t_f used in the running mean applied to the PC time series is shown in Fig. C.1e for the case $N = 10$, $\tau = 6$. For $t_f \geq 12$ months the period of POP 3 is relatively insensitive to further increases in t_f, while the decay time continues to increase (i.e. POP 3 becomes increasingly less damped). In Sections 4 and 5 $N = 10$, $\tau = 6$ and $t_f = 12$ was used.

C.2. Sensitivity of resolvent norm to the POP decay rates

As shown in Section 4.2, the resolvent norm $\| \mathscr{R}(\omega) \| = \| (i\omega \mathbf{I} - \mathbf{A})^{-1} \|$ provides a measure of the response of the system (B.1) to stochastic forcing with a frequency ω. The resonant norm of the system to forcing depends on the decay rate of each POP. As shown in Fig. C.1, the POP decay rates are sensitive to the choice of the number of EOFs used, the lag-time τ and whether or not the PC time series are smoothed prior to constructing the LIM. To further illustrate this important point, Fig. C.2 shows the resolvent norm for two additional cases based on LIMs that used unsmoothed PC time series, $\tau = 20$ months and $N = 14$ or 24 EOFs. In the case $N = 14$, $\tau = 20$ the resonant response of POP 3 is reduced compared to the case considered in Sections 4 and 5 (also shown in Fig. C.2 for reference). Conversely, increasing the number of EOFs N to 24 enhances the resonant response of not
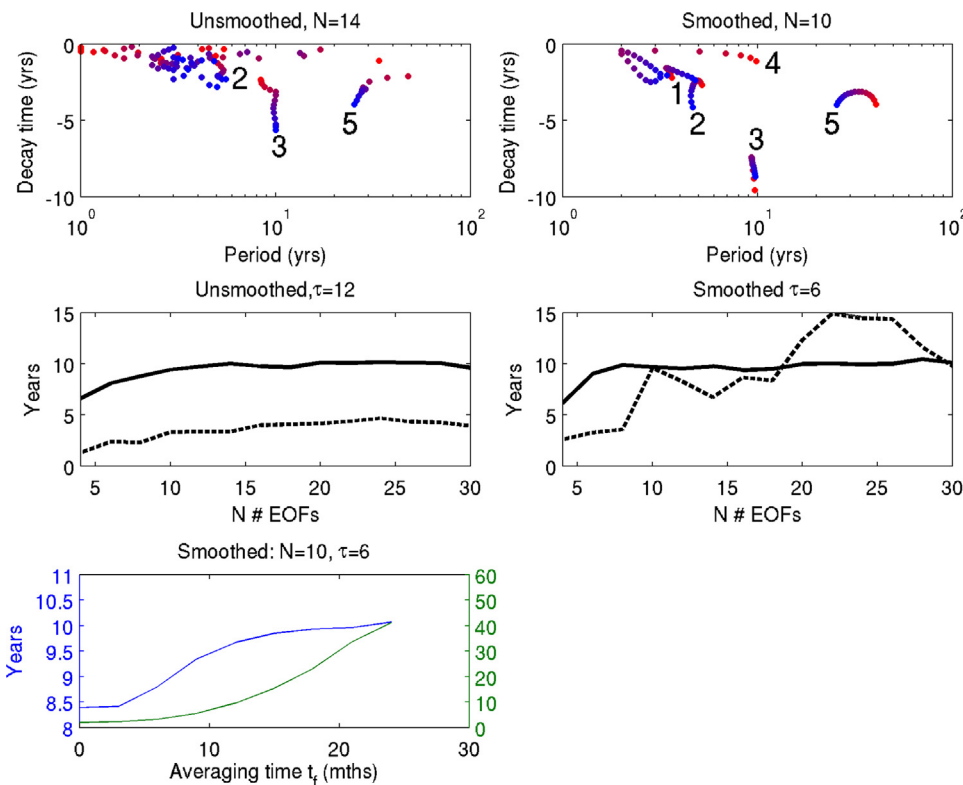

Fig. C.1. POP spectra for LIMs using (a) unsmoothed PC time series and $N = 14$, and (b) PC time series smoothed using a 12 month running mean and $N = 10$. POP frequencies are shown for τ ranging from 6 to 20 months. The color of the symbol changes gradually from red to blue over this interval. The branches labeled 1–5 correspond to the POP numbers identified in the main text. The period (solid line) and decay time (dashed line) for POP 3 versus the number of EOFs N used in the LIM are shown in (c) for the case using unsmoothed PC time series and $\tau = 12$, and (d) for the case using a 12 month running mean of the PC time series and $\tau = 6$. The period (blue) and decay time (green) of POP 3 for $N = 10$, $\tau = 6$ versus the running mean averaging period t_f (months) is shown in (e).
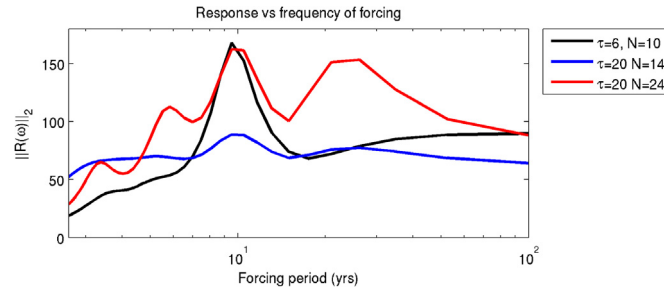
Fig. C.2. The L2-norm of the resolvent vs the forcing period for three different LIMs computed from the 4D-Var analyses for the case $N = 10$, $\tau = 6$ and smoothed PC time series (black), $N = 14$, $\tau = 20$ and unsmoothed PC time series (blue), $N = 24$, $\tau = 20$ and unsmoothed PC time series (red). Also shown is the case for a LIM computed from a long run of the model without data assimilation (black dashed).

only POP 3, but also POPs 1 and 2. An additional resonance peak appears in this case associated with POP 5 which now has a period of 23 years. For this choice of parameters POP 5 is reliable based on the coherence and phase properties of its amplitude time series (see Section 4). POP 5 appears robust for some range of parameters and deserves further investigation since Fig. 14 suggests that it could also resonate in response to the NPGO. However, POP 5 does not contribute much to the coastal upwelling variability discussed in Section 5.

C.3. Predictive skill of the LIM

An important test of any LIM is the ability of $\widetilde{\mathbf{M}}$ to predict the PC time series (Penland and Sardeshmukh, 1995; Winkler et al., 2001). Using $N = 14$, which accounts for 62% of the energy density, LIMs were constructed using $\tau = 3$, $\tau = 6$ and $\tau = 12$ months, denoted $\widetilde{\mathbf{M}}(3)$, $\widetilde{\mathbf{M}}(6)$ and $\widetilde{\mathbf{M}}(12)$ respectively. The skill of predictions (hindcasts) made by each LIM was then assessed. To ensure that each $\widetilde{\mathbf{M}}$ is independent of the data being predicted, the data during the hindcast period were withheld during the calculation of each $\widetilde{\mathbf{M}}$. Fig. C.3a shows the root mean square (rms) error in each component of $\mathbf{u}$ (i.e. the amplitude of each EOF $\mathbf{r}$) for the case of 12-month hindcasts using $\widetilde{\mathbf{M}}(12)$. The LIM is able to beat the skill of a persistence forecast for the amplitude of each EOF. It is also possible to make a 12-month forecast via two consecutive applications of $\widetilde{\mathbf{M}}(6)$ twice (i.e. using $\widetilde{\mathbf{M}}(6)^2$) or four consecutive applications of $\widetilde{\mathbf{M}}(3)$ four times (i.e. using $\widetilde{\mathbf{M}}(3)^4$). The skill of hindcasts made in this way is also shown in Fig. C.3a which shows that the forecast skill is similar to that obtained using $\widetilde{\mathbf{M}}(12)$. This demonstrates that the properties of the LIM are insensitive to the time-lag chosen. Fig. C.3b shows the rms errors for 6-month forecasts based on $\widetilde{\mathbf{M}}(6)$ and $\widetilde{\mathbf{M}}(3)^2$, while Fig. C.3c shows the rms error of 3-month forecasts based on $\widetilde{\mathbf{M}}(3)$. In all cases, the LIM is able to beat the skill of persistence, although for 3-month forecasts persistence is almost as good. Fig. C.3b also confirms that the LIM is insensitive to the time-lag, τ.
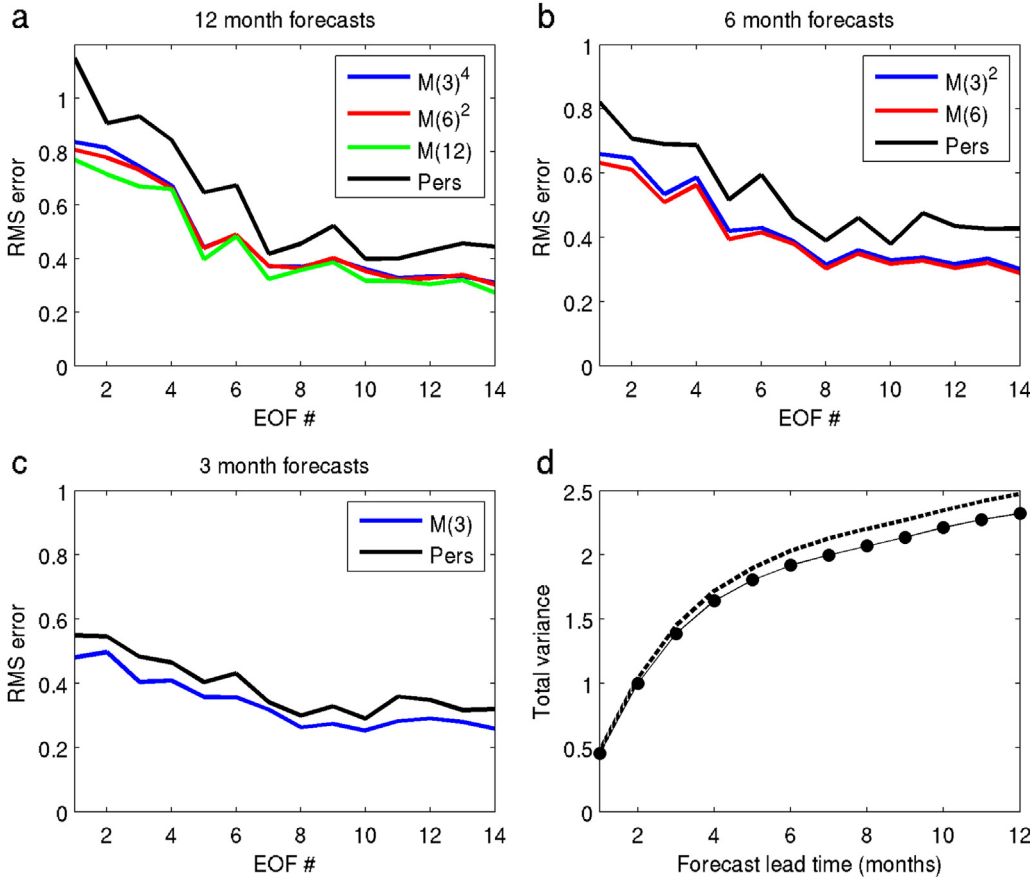

Fig. C.3. The rms error in the predicted amplitude of each EOF r for forecast lead times of (a) 12 months, (b) 6 months, and (c) 3 months for the case $N = 14$. In the case of (a) and (b) the skill of using LIMs derived from different time-lags are also shown. The skill of persistence hindcasts are shown in black. (d) The total forecast error variance vs forecast lead time computed from $\mathrm{Tr}\{\langle \varepsilon\varepsilon^T \rangle\}$ (circles) and $\mathrm{Tr}\{\mathbf{\Phi}(t) - \widetilde{\mathbf{M}}\mathbf{\Phi}(t)\widetilde{\mathbf{M}}^T\}$ (dashed curve).
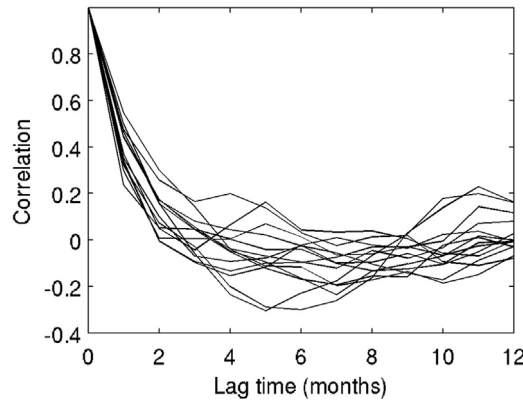
Fig. C.4. Lagged auto-correlation functions of the stochastic forcing for each principal component versus lag for the case $\tau = 12$ months, $N = 14$.

The forecast errors are given by $\varepsilon(t) = \mathbf{u}_f(t) - \mathbf{u}_t(t)$ where $\mathbf{u}_f$ and $\mathbf{u}_t$ are the forecast and true values of $\mathbf{u}$ respectively. If the $\mathbf{u}$ are consistent with (B.5), then the forecast error covariance matrix is given by $\langle \varepsilon(t) \varepsilon(t)^T \rangle = \mathbf{\Phi}(t) - \widetilde{\mathbf{M}}(t) \mathbf{\Phi}(t) \widetilde{\mathbf{M}}^T(t)$ (Penland, 1989). Fig. C.3d shows the total forecast error variance (i.e. the trace) computed from the left and right hand side of this expression as a function of the forecast interval. By and large the actual LIM forecast error variance agrees well with that expected, although it is generally under estimated, while the discrepancy between the actual and expected error variance is modest and increases with the forecast interval.

C.4. Decorrelation time of the stochastic forcing

According to (B.5), the PC time series $\mathbf{u}$ can be described as a stochastically forced linear system, where the stochastic forcing is white noise in time. White noise will decorrelate over a time interval of one time step, which for the time series considered here is one month. The stochastic forcing can be estimated by rearranging (B.5) so that $\widetilde{\boldsymbol{\xi}} dt = d\mathbf{u} - \widehat{\mathbf{A}}\mathbf{u}$ where $\widehat{\mathbf{A}}$ is the estimate of $\mathbf{A}$ based on $\widetilde{\mathbf{M}}$ in (B.6), and $\mathbf{u}$ is the actual vector of PC time series. Fig. C.4 shows the time-lagged auto-correlation versus lag time of the stochastic forcing for each component of $\mathbf{u}$ for the case $\tau = 12$ months and $N = 14$. In most cases the lag-1 correlation decreases rapidly, indicating that the assumption of white noise forcing in time is reasonable for this system.

C.5. Stochastic forcing covariance

The covariance matrix of the stochastic forcing $\boldsymbol{\xi}$ in (B.1) obeys the Lyapunov equation:

$$\mathbf{A}\mathbf{C}(t) + \mathbf{C}(t)\mathbf{A}^T + \mathbf{Q} = 0 \tag{C.1}$$

where $\mathbf{Q} = \langle \boldsymbol{\xi} \boldsymbol{\xi}^T \rangle dt$ (Antoulas, 2005). Eq. (C.2) is also referred to as the fluctuation-dissipation relation by Penland and Sardeshmukh (1995) following Gardiner (1985). Using (B.6), the covariance matrix of the stochastic forcing can be estimated according to:

$$\widetilde{\mathbf{Q}} = -(\widehat{\mathbf{A}}\mathbf{\Phi}(t) + \mathbf{\Phi}(t)\widehat{\mathbf{A}}^T). \tag{C.2}$$

Another indicator of the veracity of the LIM is the eigenspectrum $\widetilde{\mathbf{Q}}$ which should be a positive-definite matrix. For example, for the test case considered here with $\tau = 12$ months and $N = 14$, $\widetilde{\mathbf{Q}}$ has two negative eigenvalues. The presence of negative eigenvalues does not negate the hypotheses of the LIM, but rather is an indicator of the influence of various approximations and uncertainties, such as unreliable higher order EOFs, or where (B.1) is only approximately valid (see Penland and Sardeshmukh, 1995 and Del Sole and Hou, 1999 for further discussion). When properties of the stochastic forcing are sought using $\widetilde{\mathbf{Q}}$, it is usual to disgard the eigenvectors of $\widetilde{\mathbf{Q}}$ with negative eigenvalues. In the cases presented in Sections 4 and 5, we use $\tau = 6$ months and $N = 10$ and the PC time series were detrended and smoothed in time using a 12-month running mean. In this case, all of the eigenvalues of $\widetilde{\mathbf{Q}}$ are positive. Fig. C.5 shows the percentage variance explained by the eigenvectors (EOFs) of $\widetilde{\mathbf{Q}}$ computed from (C.2) and
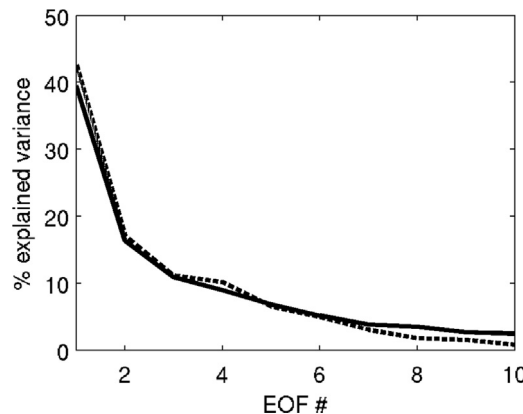

Fig. C.5. Percentage variance explained by the eigenvectors of $\mathbf{Q}_e$ (solid line) and $\widetilde{\mathbf{Q}}$ (dashed line).

$\mathbf{Q}_e$, the covariance matrix of the actual stochastic forcing computed from $d\mathbf{u} - \widehat{\mathbf{A}}\mathbf{u}$. The eigenspectra of $\widetilde{\mathbf{Q}}$ and $\mathbf{Q}_e$ are clearly very similar, lending further weight to the underlying hypotheses of (B.1). In addition, the leading EOFs of $\widetilde{\mathbf{Q}}$ and $\mathbf{Q}_e$ are very similar (not shown), although $\mathrm{Tr}(\mathbf{Q}_e) \sim 0.2\,\mathrm{Tr}(\widetilde{\mathbf{Q}})$ indicating that (C.2) tends to significantly over estimate the total variance of the stochastic forcing.

References

Antoulas, A.C., 2005. Advances in design and control, society for industrial and applied mathematics. Approx. Large-Scale Dyn. Syst. 479.

Atlas, R., Hoffman, R.N., Ardizzone, J., Leidner, S.M., Jusem, J.C., Smith, D.K., Gombos, D., 2011. A cross-calibrated, multiplatform ocean surface wind velocity product for meteorological and oceanographic applications. Bull. Am. Meteor. Soc. 92, 157–174. http://dx.doi.org/10.1175/2010BAMS2946.1.

Bograd, S.J., Lynn, R.J., 2003. Long-term variability in the Southern California Current System. Deep Sea Res. Part II: Top. Stud. Oceanogr. 50, 2355–2370. http://dx.doi.org/10.1016/S0967-0645(03)00131-0.

Carton, J.A., Giese, B.S., 2008. A reanalysis of ocean climate using simple ocean data assimilation (SODA). Mon. Weather Rev. 136, 2999–3017.

Chavez, F.P., Ryan, J., Lluch-Cota, S.E., Ñiquen, M.C., 2003. From Anchovies to Sardines and Back: multidecadal change in the Pacific Ocean. Science 299, 217–221. http://dx.doi.org/10.1126/science.1075880.

Chenillat, F., Riviére, P., Capet, X., Di Lorenzo, E., Blanke, B., 2012. North Pacific Gyre Oscillation modulates seasonal timing and ecosystem functioning in the California Current upwelling system. Geophys. Res. Lett. 39, L01606. http://dx.doi.org/10.1029/2011GL049966.

Chhak, K., Di Lorenzo, E., 2007. Decadal variations in the California Current upwelling cells. Geophys. Res. Lett. 34, L14604. http://dx.doi.org/10.1029/2007GL030203.

Chhak, K.C., Di Lorenzo, E., Schneider, N., Cummins, P.F., 2009a. Forcing of low-frequency ocean varuiability in the Northeast Pacific. J. Clim. 22, 1255–1276.

Chhak, K.C., Moore, A.M., Milliff, R.F., 2009b. Stochastic forcing of ocean variability by the North Atantic Oscillation. J. Phys. Oceanogr. 39, 162–184.

Combes, V., Chenillat, F., Di Lorenzo, E., Rivi?re, P., Ohman, M.D., Bograd, S.J., 2013. Cross-shore transport variability in the California Current: Ekman upwelling vs. eddy dynamics. Prog. Oceanogr. 109, 78–89. http://dx.doi.org/10.1016/j.pocean.2012.10.001.

Dee, D.P., et al., 2011. The ERA-Interim reanalysis: configuration and performance of the data assimilation system. Q.J.R. Meteorol. Soc. 137, 553–597. http://dx.doi.org/10.1002/qj.828.

Del Sole, T., Hou, A.Y., 1999. Empirical stochastic models of the dominant climate statistics of a general circulation model. J. Atmos. Sci. 56, 3436–3456.

Di Lorenzo, E., Fiechter, J., Schneider, N., Bracco, A., Miller, A.J., Franks, P.J.S., Bograd, S.J., Moore, A.M., Thomas, A.C., Crawford, W., Peña, A., Hermann, A.J., 2009. Nutrient and salinity decadal variations in the central and eastern North Pacific. Geophys. Res. Lett. 36, L14601. http://dx.doi.org/10.1029/2009GL038262.

Di Lorenzo, E.,.N., Schneider, K.M., Cobb, P.J.S., Franks, K., Chhak, A.J., Miller, J.C., McWilliams, S.J., Bograd, H., Arango, E., Curchitser, T.M., Powell, Rivíere, P., 2008. North Pacific Gyre Oscillation links ocean climate and ecosystem change. Geophys. Res. Lett. 35, L08607. http://dx.doi.org/10.1029/2007GL032838.

Dommenget, D., Latif, M., 2002. A cautionary note on the interpretation of EOFs. J. Clim. 15, 216–225.

Farrell, B.F., Ioannou, P.J., 1996. Generalized stability theory. Part I: autonomous operators. J. Atmos. Sci. 53, 2025–2040.

Field, D., Cayan, D., Chavez, F., 2006. Secular warming in the California Current and North Pacific. CalCOFI Rep. 47, 92–108.

Gardiner, C.W., 1985. Handbook of Stochastic Methods, 2nd ed. Springer, Berlin, pp. 444.

Golub, G.H., Van Loan, C.F., 1989. Matrix Computations. Johns Hopkins University Press, Baltimore.

Hasslemann, K., 1988. PIPs and POPs - a general formalism for the reduction of dynamical systems in terms of principal interaction patterns and principal oscillation patterns. J. Geophys. Res. 93, 11015–11020.

Jacox, M.G., Moore, A.M., Edwards, C.A., Fiechter, J., 2014. Spatially resolved upwelling in the California Current system and its connections to climate variability. Geophys. Res. Lett. 41, 3189–3196. http://dx.doi.org/10.1002/2014GL059589.

Jacox, M.G., Fiechter, J., Moore, A.M., Edwards, C.A., 2015. El Niño and the California current coastal upwelling response. J. Geophys. Res. 120. http://dx.doi.org/10.1002/2014JC010650.

Johnstone, J.A., Mantua, N.J., 2014: Atmospheric controls on northeast Pacific temperature variability and change, 1900–2012. In: Proceedings of the National Academy of Sciences, 111, pp. 14360–14365.

Källberg, P.A., Simmons, A., Uppala, S., 2004. The ERA-40 Archive. ERA-40 Project Report Series No. 17.

Kelly, K.A., Beardsley, R.C., Limeburner, R., Brink, K.H., Paduan, J.D., Chereskin, T.K., 1998. Variability of the near-surface eddy kinetic energy in California Current based on altimetric, drifter, and moored current data. J. Geophys. Res. 103, 13,067–13,083.

King, J.R., 2005. Report of the Study Group on Fisheries and Ecosystem Responses to Recent Regime Shifts. PICES Scientific Report No. 28.

Kleeman, R., Moore, A.M., 1997. A theory for the limitations of ENSO predictability due to stochastic atmospheric transients. J. Atmos. Sci. 54, 753–767.

Macias, D., Landry, M.R., Gershunov, A., Miller, A.J., Franks, P.J.S., 2012. Climate control of upwelling variability along the western north-American coast. PLoS One 7, e30436.

Mantua, N.J., Hare, S.R., Zhang, Y., Wallace, J.M., Francis, R.C., 1997. A Pacific interdecadal climate oscillation with impacts on salmon production Bull. Am. Met. Soc. 78, 1069–1079.

McClatchie, S., et al., 2009. The state of the California Current, 2007–2008: La Niña conditions and their effects on the ecosystem. CalCOFI Rep. 49, 39–76.

McGowan, J.A., Bograd, S.J., Lynn, R.J., Miller, A.J., 2003. The biological response to the 1977 regime shift in the California Current. Deep Sea Res. Part II: Top. Stud. Oceanogr. 50, 2567–2582. http://dx.doi.org/10.1016/S0967-0645(03)00135-8.

Miller, A.J., Cayan, D.R., Barnett, T.P., Graham, N.E., Oberhuber, J.M., 1994. The 1976–77 climate shift of the Pacific Ocean. Oceanography 7, 21–26. http://dx.doi.org/10.5670/oceanog.1994.11.

Monahan, A.H., Fyfe, J.C., 2006. On the nature of zonal jet EOFs. J. Clim. 19, 6409–6424.

Monahan, A.H., Fyfe, J.C., Ambaum, M.H.P., Stephenson, D.B., North, G.R., 2009. Empirical orthogonal functions: the medium is the message. J. Clim. 22, 6501–6514.

Moore, A.M., Kleeman, R., 2001. On the differences between the optimal perturbations of coupled models of ENSO. J. Clim. 14, 138–163.

Moore, A.M., Arango, H.G., Di Lorenzo, E., Cornuelle, B.D., Miller, A.J., Neilson, D.J., 2004. A comprehensive ocean prediction and analysis system based on the tangent linear and adjoint of a regional ocean model. Ocean Model. 7, 227–258.

Moore, A.M., Jacox, M.G., Crawford, W.J., Laughlin, B., Edwards, C.A., Fiechter, J., 2017. The Impact of the ocean observing system on estimates of the California Current circulation spanning three decades. Prog. Oceanogr. http://dx.doi.org/10.1016/j.pocean.2017.05.009.

Neveu, E., Moore, A.M., Edwards, C.A., Fiechter, J., Drake, P., Crawford, W.J., Jacox, M.G., Nuss, E., 2016. An historical analysis of the California Current using ROMS 4D-Var. Part I: System configuration and diagnostics. Ocean Model 99, 131–151. http://dx.doi.org/10.1016/j.ocemod.2015.11.012.

Newman, M., Compo, G.P., Alexander, M.A., 2003. ENSO forced variability of the Pacific decadal oscillation. J. Clim. 16, 3853–3857.

North, G.R., Bell, T.L., Cahalan, R.F., Moeng, F.J., 1982. Sampling errors in the estimation of empirical orthogonal functions. Mon. Weather Rev. 110, 699–706.

Pedlosky, J., 1979. Geophysical Fluid Dynamics. Springer-Verlag, New York, pp. 710.

Penland, C., 1989. Random forcing and forecasting using principal oscillation pattern analysis. Mon. Weather Rev. 117, 2165–2185.

Penland, C., Ghil, M., 1993. Forecasting hemisphere 700 mb geopotential heights using principal oscillation patterns. Mon. Weather Rev. 121, 2355–2372.

Penland, C., Magorian, T., 1993. Prediction of Niño-3 sea surface temperatures using linear inverse modeling. J. Clim. 6, 1067–1076.

Penland, C., Sardeshmukh, P.D., 1995. The optimal growth of tropical sea surface temperature anomalies. J. Clim. 8, 1999–2024.

Schneider, N., Cornuelle, B.D., 2005. The forcing of the Pacific Decadal Oscillation. J. Clim. 18, 4355–4373.

von Storch, H., Bürger, G., Schnur, R., von Storch, J.-S., 1995. Principal oscillation patterns: a review. J. Clim. 8, 377–400.

Winkler, C.R., Newman, M., Sardeshmukh, P.D., 2001. A linear model of wintertime low-frequency variability. Part I: formulation and forecast skill. J. Clim. 14, 4474–4494.

Wolter, K., Timlin, M.S., 2011. El Niño/southern oscillation behaviour since 1871 as diagnosed in an extended multivariate ENSO index (MEI.ext). Int. J. Clim. 31, 1074–1087.